On the cumulus diurnal cycle over the tropical warm pool

James H. Ruppert, Jr.,[1,2] Richard H. Johnson[1]

Diurnally varying sea surface temperature and direct radiative heating exert distinct influences on cumulus convection

Cloud-layer moistening is critical to the development of precipitating convection

Mesoscale cloud organization is highly modulated as a function of diurnal rainfall

---

Corresponding author: James H. Ruppert, Jr., Max Planck Institute for Meteorology, Hamburg, Germany. (james.ruppert@mpimet.mpg.de)

[1]Department of Atmospheric Science,
Colorado State University, Fort Collins,
Colorado, USA.

[2]Max Planck Institute for Meteorology,
Hamburg, Germany (current affiliation).

This article has been accepted for publication and undergone full peer review but has not been through the copyediting, typesetting, pagination and proofreading process which may lead to differences between this version and the Version of Record. Please cite this article as an 'Accepted Article', doi: 10.1002/2015MS000610

Abstract.

An idealized cloud-resolving model experiment is executed to study the prominent cumulus diurnal cycle in suppressed regimes over the tropical warm pool. These regimes are characterized by daytime cumulus invigoration and cloud-layer moistening connected with enhanced diurnal cycles in shortwave radiative heating (SW) and sea surface temperature (SST). The relative roles of diurnally varying SW and SST in this cumulus diurnal cycle are assessed, wherein radiation is modeled and SST is prescribed. Large-scale subsidence is parameterized using the spectral weak temperature gradient (WTG) scheme, such that large-scale vertical motion (w_{wtg}), and hence subsidence drying, is modulated by diurnal changes in diabatic heating. A control simulation exhibits daytime cumulus invigoration that closely matches observations, including midday cloud-layer moistening. This cumulus invigoration is composed of two distinct modes: 1) a midday non-precipitating ("forced") mode of predominately shallow clouds, driven by the peak in SST and surface fluxes as the mixed layer deepens and dries; and 2) a precipitating late-afternoon ("active") mode characterized by deeper clouds in connection with a more moist cloud layer. This cloud-layer moistening is driven by the daytime relaxation of w_{wtg} subsidence, which is prompted by the midday peak in SW. The transition from the surface flux-driven forced mode to the active precipitating mode is accompanied by a transition from relatively small-scale boundary layer circulation cells to larger cells that are highly modulated by cold pools, consistent with observations. When the diurnal cycle is removed,

clouds are persistently shallower with virtually no rainfall, emphasizing the inherent nonlinearity of the cumulus diurnal cycle.

1. Introduction

Regimes of shallow moist convection in the tropical warm pool region exhibit a pronounced diurnal cycle, with corresponding daytime increases in cloud depth and moisture in the low–midtroposphere (Fig. 1) [*Chen and Houze*, 1997; *Sui et al.*, 1997; *Johnson et al.*, 2001; *Bellenger et al.*, 2010; *Ruppert and Johnson*, 2015]. In such regimes, the diurnal cycles of shortwave radiative heating (SW) and sea surface temperature (SST) are at their maximum amplitude, and hence both direct radiative forcing and SST-driven increases in air–sea fluxes may play important roles in this diurnal cycle [*Webster et al.*, 1996; *Weller and Anderson*, 1996; *Chen and Houze*, 1997; *Sui et al.*, 1997; *Johnson et al.*, 2001; *Bellenger et al.*, 2010; *Ruppert and Johnson*, 2015]. The relative, distinct roles of SST and direct radiative forcing in the cumulus diurnal cycle, however, have not been assessed.

Ruppert and Johnson [2015] (hereafter, RJ15) hypothesize that this shallow cumulus diurnal cycle and the associated diurnal cloud-layer moistening rectifies onto longer timescales, in that this diurnal cycle drives deeper clouds and greater moistening in the daily-mean sense than would otherwise occur. This study aims to understand the driving mechanism(s) in the cumulus diurnal cycle, and the relative roles of 1) direct radiative heating and 2) SST therein. This assessment will help elucidate the nonlinearity of the cumulus diurnal cycle, and in turn, bring us closer to understanding how the cumulus diurnal cycle fits into the greater climate system.

Observations reveal that regimes of organized deep moist convection over the tropical oceans exhibit a pronounced diurnal cycle (i.e., distinct from land influences), with a

prominent predawn rainfall peak [*Gray and Jacobson*, 1977]. The exact mechanism that accounts for this diurnal rainfall phasing is still debated [*Randall et al.*, 1991; *Mapes and Houze*, 1993; *Xu and Randall*, 1995; *Chen and Houze*, 1997; *Liu and Moncrieff*, 1998; *Dai*, 2001; *Yang and Slingo*, 2001; *Woolnough et al.*, 2004; *Yang and Smith*, 2006; *Nicholls*, 2015]. Convective systems in such regimes tend to first initiate during the day, and build through the afternoon and night [*Mapes and Houze*, 1993; *Chen and Houze*, 1997; *Sui et al.*, 1997; *Bellenger et al.*, 2010]. This daytime invigoration is often attributed to the diurnal cycle of SST and the associated cycle in surface fluxes [*Chen and Houze*, 1997; *Johnson et al.*, 2001; *Bellenger et al.*, 2010] [RJ15]. When deep convection is suppressed by large-scale subsidence – as in undisturbed or suppressed regimes – the diurnal SST cycle and daytime convective invigoration are more prominent, although a distinct nocturnal cloud maximum often remains (Fig. 1) [*Sui et al.*, 1997; *Johnson et al.*, 2001; *Bellenger et al.*, 2010] [RJ15]. The nocturnal cloud signal in suppressed regimes may be linked to diurnal tides [*Woolnough et al.*, 2004], and is not the focus of this study.

The diurnal cycle in SST can at times exceed 3°C in magnitude under suppressed large-scale conditions, owing to the formation of surface diurnal warm layers, as follows: oceanic convection is suppressed as the upper ocean becomes stabilized under strong daytime insolation and light surface wind speed (i.e., $<$6 m s^{-1}), leading to increasingly concentrated solar warming, and hence a sharp daytime SST increase [*Halpern and Reed*, 1976; *Price et al.*, 1986; *Stramma et al.*, 1986; *Webster et al.*, 1996; *Soloviev and Lukas*, 1997; *Bernie et al.*, 2005; *Shinoda*, 2005; *Clayson and Bogdanoff*, 2013; *Matthews et al.*, 2014]. The daytime increase in surface fluxes, in turn, is driven by the diurnal increase of SST and wind speed in the planetary boundary layer (PBL) (Fig. 1) [*Johnson et al.*,

2001; *Bellenger et al.*, 2010]. Convection is invigorated by this increase in surface fluxes, which deepens the mixed layer [*Johnson et al.*, 2001]; hence, to some measure this diurnal cycle is analogous to that over land (Fig. 1) [*Grabowski et al.*, 2006; *Khairoutdinov and Randall*, 2006; *Bellenger et al.*, 2010].

In addition to SST forcing, radiative heating also plays a more direct role in the diurnal cycle of convection. Although this topic is unresolved (see the review by *Yang and Smith* [2006]), there are two preeminent schools of thought: 1) a baroclinic circulation arises from nocturnally enhanced radiative cooling in clear regions relative to adjacent cloudy regions (during the day, the regions may both experience negligible radiative cooling) [*Gray and Jacobson*, 1977]; and 2) convection is locally modulated by the diurnal SW cycle and its direct effect on lapse rate through cloud absorption [*Randall et al.*, 1991; *Xu and Randall*, 1995]. Both of these mechanisms are likely active in nature, although to what extent is a function of the convective regime. *Liu and Moncrieff* [1998] argue that in transient, fast-moving oceanic convective systems, the direct radiative lapse rate mechanism dominates. When cloud systems are more stationary and organized on larger scales, however, the differential radiative cooling/warming mechanism may dominate. In tropical cyclones, for instance, *Nicholls* [2015] argues that enhanced nocturnal radiative cooling adjacent to the cloud shield augments ascent and moistening within the cyclone core overnight, leading to nocturnal intensification. This argument is consistent with the findings from case studies [*Dunion et al.*, 2014; *Melhauser and Zhang*, 2014].

The differential radiative heating/cooling mechanism implies that in the suppressed environment adjacent to large and/or slow-moving regions of organized deep convection, subsidence is weakest during the day and strongest at night. Observations from the 2011–

12 DYNAMO field experiment (Dynamics of the Madden Julian Oscillation, or MJO; *Madden and Julian* [1971, 1972]) are consistent with this notion. During DYNAMO suppressed regimes, large-scale subsidence was observed to peak nocturnally, with relaxed subsidence or weak ascent during the day [RJ15]. Such a signal may reflect diurnal pulsation of the ITCZ, which, during DYNAMO, was positioned several hundred kilometers to the south of the sounding array. Large-scale surface wind observations are consistent with this notion [*Dai and Deser*, 1999; *Gille et al.*, 2003]. This diurnal cycle in large-scale motion is also consistent with weak temperature gradient (WTG) theory, which emphasizes the observed first-order balance between diabatic heating and large-scale adiabatic warming/cooling in the tropics [*Sobel and Bretherton*, 2000; *Sobel et al.*, 2001; *Yano and Bonazzola*, 2009]. Given this balance, enhanced nocturnal radiative cooling implies strengthened subsidence, while increased shortwave heating implies relaxed subsidence during the day.

An aspect of the shallow cumulus diurnal cycle found during DYNAMO suppressed regimes is the daytime moistening of the low–midtroposphere that corresponds with cloud deepening (Fig. 1) [RJ15]. RJ15 speculate that this moistening is driven by the midday peak in SST via the convective invigorated by surface fluxes. Ascertaining cause and effect, however, is difficult from the observations alone. This diurnal moistening is an issue of special emphasis in this study, given possible implications of this moistening for longer timescales [RJ15].

In this study, the relative, direct roles of SST and radiative heating are assessed in the cumulus diurnal cycle over the warm pool using an idealized model framework at cloud-resolving scales. The assumption that large-scale vertical motion is in (i.e., relaxed toward)

WTG balance is made *a priori*; hence, diurnally varying large-scale subsidence is implicitly represented as a response to diurnally varying diabatic heating. Model techniques and experiment methodology are provided in section 2, with results in section 3, and summary and conclusions in section 4.

2. Experiment and Analysis Methodology

2.1. Model Framework

Of paramount importance for this experiment is the explicit treatment of moist convection and the feedbacks between clouds, surface fluxes, and radiative heating that collectively drive the cumulus diurnal cycle. A suite of cloud-resolving model simulations is therefore executed with Cloud Model 1 (CM1; release 17), which solves the mass- and energy-conserving system of equations for moist processes [*Bryan and Fritsch*, 2002; *Bryan et al.*, 2003]. The model grid is discretized as follows: $\Delta x = \Delta y = 200$ m; $\Delta z = 50$ m for $0 \leq z \leq 2$ km, and $\Delta z = 350$ m for $z > 15$ km, with the smooth stretching function of *Wilhelmson and Chen* [1982] applied for $2 < z \leq 15$ km. Thus, there are 40 vertical levels in the lowest 2 km. Model top is at 22 km, with 125 vertical levels in total. Since boundary-layer development and vertical convective mixing are explicitly resolved at this grid scale, no boundary layer scheme is employed, and instead subgrid-scale turbulence is modeled following *Deardorff* [1980]; thus, this framework is similar to a large eddy simulation (LES) framework [*Bryan et al.*, 2003]. An additional simulation executed with 100-m horizontal spacing (otherwise identical to the control) yielded virtually identical results to the simulations shown in this study, suggesting that convergence of the solution is achieved with this model grid.

CM1 employs the third-order Runge–Kutta (RK) time-splitting integration scheme [*Wicker and Skamarock*, 2002], using an adaptive large time step ($\Delta t \sim 5$ s). A compressible, vertically implicit pressure solver is employed [*Klemp et al.*, 2007] with fifth-order advection (no artificial diffusion necessary) [*Wicker and Skamarock*, 2002]. Microphysics is modeled using the *Morrison et al.* [2005, 2009] scheme. This scheme is two-moment in rain water, cloud ice, snow, and graupel, with only the mass of cloud water predicted (assumed cloud droplet concentration $N_d = 100$ cm^{-3}; as in *Li et al.* [2015]). The equations for rain droplet autoconversion and accretion have been updated to those of *Kogan* [2013]. Please refer to other studies for microphysical sensitivity tests [*Stevens and Seifert*, 2008; *VanZanten et al.*, 2011; *Li et al.*, 2015].

Although an ocean mixed-layer model can be employed to represent the diurnal SST cycle [*Webster et al.*, 1996; *Bernie et al.*, 2005; *Matthews et al.*, 2014], SST is instead prescribed to isolate the ocean forcing on clouds. SST is represented by a repeating diurnal composite from 10-min SST measurements taken at the R/V *Revelle* during the Nov 2011 MJO suppressed phase in DYNAMO (13–15 Nov; denoted SP/MJO2, hereafter). The DYNAMO SST dataset is comprised by near-surface SeaSnake temperature measurements with the cool-skin correction applied [*Fairall et al.*, 1996; *Moum et al.*, 2013]. The diurnal composite was generated from this dataset, and was smoothed using a 30-min running-mean window. The composite diurnal SST range is $\sim$2°C (Fig. 5). Although the diurnal cycle was also prominent during the suppressed phase of the Oct MJO in DYNAMO (SP/MJO1; Fig. 1, left), the diurnal cycle of SST as measured at the *Revelle* was much weaker. Therefore, SP/MJO2 is employed as the primary observational reference in this study. The surface fluxes of heat and moisture are calculated from the bulk formulae

assuming constant surface exchange coefficients ($C_h = 1.66 \times 10^{-3}$ and $C_q = 1.74 \times 10^{-3}$ for heat and moisture, respectively), which were derived from the SP/MJO2 *Revelle* flux measurements [*Moum et al.*, 2013]. Radiative fluxes are simulated using the NASA Goddard longwave and shortwave radiation schemes, which are cloud-interactive [*Chou and Suarez*, 1994, 1999; *Tao et al.*, 1996]. The day is held fixed to 13 Nov 2011 in the solar zenith angle calculations (lateral cloud shading is excluded) to prevent seasonal advancement. The location is set to 0°, 80°E (i.e., the location of the R/V *Revelle* in DYNAMO). Radiative fluxes are computed every five minutes.

The model base state is homogeneously prescribed using the sounding shown in Fig. 2, which is an idealization of the mean R/V *Revelle* sounding for SP/MJO2 (i.e., thin features in temperature and humidity that were deemed spurious, by comparison with various time ranges and other sounding sites, were removed). Tests carried out offline demonstrate very little sensitivity to this idealization procedure. The model sounding is characterized by a shallow mixed layer with relative humidity (RH) increasing from ∼70% to ∼95% from the surface to mixed-layer top, similar to mixed layers documented in suppressed periods during COARE (the Coupled Ocean–Atmosphere Response Experiment) [*Johnson et al.*, 2001]. RH decreases above the mixed layer to a minimum of ∼25% around 300 hPa. It again increases upwards from 300 hPa. The sounding is characterized by appreciable convective instability, with CAPE (convective available potential energy) of 1580 J kg^{-1}. Zonal wind (u) is initialized as shown, with no initial meridional wind. u increases from 1.5 to 3 m s^{-1} from the surface to ∼850 hPa, to 4 m s^{-1} by 400 hPa, and finally to 8 m s^{-1} by ∼275 hPa. Wind speed above this level has been highly simplified, since the results are insensitive to wind at such altitudes (clouds remain shallow in the simulations; Fig. 5).

Since surface drag is imposed, horizontal velocity is maintained by relaxing the winds toward the base-state profile using a relaxation timescale $\tau = 24$ h (to permit diurnal variations). Random perturbations of $\leq$0.1 K in amplitude are applied ubiquitously to potential temperature θ in the base state to initialize three-dimensional motion.

Since the model wind field is dominated by u, the domain accommodates cloud system development over a large swath by employing a 102.4-km zonal dimension, with a 48-km meridional dimension. Differences were negligible among a series of offline tests in which the horizontal domain shape and size were modified (e.g., a simulation with x- and y-dimensions both of 32 km). Periodic lateral boundary conditions are imposed. Rayleigh damping is applied for $z > 18.5$ km (9 vertical levels). Computations for the 15.36 million grid points are divided over 32 (24) processors in x (y), and executed on the NCAR Yellowstone (http://n2t.net/ark:/85065/d7wd3xhc) supercomputing system.

2.2. WTG Scheme

In the deep tropics, the Coriolis torque is very weak, and gravity waves (or buoyancy bores; *Mapes* [1993]) effectively disperse local temperature anomalies, thus keeping temperature gradients and local variations very weak [*Charney*, 1963; *Mapes and Houze*, 1995; *Yano and Bonazzola*, 2009]. The resulting first-order balance – weak temperature gradient (WTG) balance – is between adiabatic warming/cooling and diabatic heat sinks/sources [*Sobel and Bretherton*, 2000; *Sobel et al.*, 2001]. In suppressed regimes, for example, the dominant balance is between radiative cooling and subsidence warming, which in turn drives the subsidence drying that maintains convection in a shallow state [*Nitta and Esbensen*, 1974; *Johnson and Lin*, 1997; *Mapes*, 2001; *Takemi et al.*, 2004] [RJ15]. WTG theory implicitly assumes the dispersion of local temperature anomalies by gravity waves,

which adjust large-scale vertical motion to maintain temperature. Given this assumption, WTG theory enables the parameterization of large-scale vertical motion, e.g., in a limited-area model, which acts to offset the heating/cooling due to simulated diabatic processes.

WTG parameterizations act to keep domain-averaged temperature fixed to, or relaxed toward, a given reference profile, $\theta_0(z)$, which is assumed to be representative of the large-scale environment. This is achieved by diagnosing the vertical motion required to offset temperature anomalies, via adiabatic motion, that arise from simulated diabatic sources [*Sobel and Bretherton*, 2000; *Raymond and Zeng*, 2005]. This "external," one-dimensional profile of large-scale vertical motion w_{wtg} is then used to advect temperature and humidity (externally from the advection procedures of the model core), thus keeping temperature fixed over time, and coupling humidity to the diabatic heat source. In this study, the spectral WTG scheme of *Herman and Raymond* [2014] is implemented in CM1. This scheme is a specific implementation of relaxed WTG [*Raymond and Zeng*, 2005], wherein small, transient temperature anomalies can develop. This spectral WTG scheme accounts for the mode-dependency of buoyancy bores; namely, the proportionality between the propagation rate of buoyancy bores and the vertical depth of their parent buoyancy anomalies [*Nicholls et al.*, 1991; *Mapes*, 1993]. Therefore, shallow domain-averaged temperature anomalies yield a slower relaxation toward $\theta_0(z)$ than deep temperature anomalies (see *Herman and Raymond* [2014] for more details). Small diurnally-generated temperature anomalies can therefore arise and impact the convection.

Using the same WTG scheme, *Sentić et al.* [2015] demonstrate that the evolution of precipitation, lapse rate, and humidity during DYNAMO are well-represented by the WTG

framework. Comparison between measured vertical motion (w_{dynamo}) and WTG-balanced vertical motion from DYNAMO during SP/MJO2 (i.e., $w_{balanced}$) further supports that WTG is a reasonable approximation for this period (Fig. 3) [$w_{balanced} = Q_1(d\overline{\theta}/dz)^{-1}$, where Q_1 is the apparent heat source for SP/MJO2, and the over-line indicates a horizontal domain average] (the profile from the control simulation, w_{ctl}, is discussed in more detail later). See *Johnson et al.* [2015] for details on the vertical motion calculation from DYNAMO observations.

The procedure for applying the spectral WTG scheme, as implemented in CM1, is as follows. $\theta_0(z)$ should be representative of the large-scale environment of study; this is therefore chosen to be the mean sounding from SP/MJO2, as used for the base state (Fig. 2). The same is applied for all sensitivity tests. *Sentić et al.* [2015] also employed DYNAMO soundings to represent a time-varying reference state as a function of MJO phase. The simulated input information for the WTG scheme [i.e., $\overline{\theta}(z,t)$] is first interpolated onto a vertical grid of constant 50-m spacing. The profile of WTG vertical motion w_{wtg} is then diagnosed from the spectral WTG scheme, interpolated back onto the stretched vertical grid, and masked in the boundary layer (see below). Finally, w_{wtg} is then used to advect θ and water vapor mixing ratio q in each model column using second-order differencing. w_{wtg} is updated every 300 s.

A current issue with WTG parameterizations is that w_{wtg} does not hold in the PBL where static stability is small and temperature variations can be large [*Johnson et al.*, 2001; *Raymond and Zeng*, 2005; *Herman and Raymond*, 2014]. Therefore, a mean profile of vertical motion from the DYNAMO northern sounding array averaged over SP/MJO2

is used to mask w_{wtg} near the surface (i.e., w_{dynamo}; Fig. 3). This masking is complete from 0–0.5 km, linearly decreased from 0.5–1.5 km, and absent above 1.5 km.

2.3. Experimental Design

A suite of model sensitivity tests is executed to both isolate and better understand the distinct cumulus forcing by the diurnal variations in 1) SST and 2) direct radiative heating. These two diurnal forcing mechanisms serve as the two primary control variables. The model tests are listed in Table 1. The control (CTL) includes both the radiative and SST diurnal mechanisms, with the diurnal cycle of SST prescribed homogeneously (as described in section 2.1). FIXSW is identical to CTL except with the diurnal cycle of SW removed by fixing the time to 0621L (local time) in the zenith calculation of the radiation scheme. This is equivalent to prescribing the incoming SW to the diurnal mean, given that lateral cloud shading is excluded from the radiation scheme. FIXSST is identical to CTL except with SST fixed to the diurnal mean of 29.9°C. In NODC, both diurnal modes are removed following these methods. DBLSST is identical to CTL except with the diurnal amplitude of SST doubled (i.e., ∼4°C). Although this diurnal SST magnitude is more rare, similar values were observed in calm-wind conditions during COARE [*Soloviev and Lukas*, 1997]. DBLSST emphasizes and hence sheds light on the direct cumulus response to SST forcing. Finally, in XCLDRAD, all species of water aside from vapor are set to zero in the input to the radiation scheme, thereby removing direct cloud–radiative feedbacks. XCLDRAD is otherwise identical to CTL.

Each simulation is initialized at local midnight and integrated for sixteen days, with the radiative tendencies ramped up linearly from zero over the first 12 h to allow the cloud field to initialize before w_{wtg} fully spins up. As will be shown, the simulated diurnal

cycle is virtually identical from day to day (after a one-day spin-up), and thus results are only shown for the first eight days, and for only three selected days when greater detail is emphasized. Model output is analyzed and presented at 30-min frequency.

In DYNAMO suppressed periods, moisture above the cumulus layer was sustained by horizontal-advective moistening [*Sobel et al.*, 2014]. Without this advective source, subsidence would dry the mid–upper troposphere and low–midlevel longwave cooling would amplify, in turn amplifying the subsidence (via WTG balance), and so on, until moist convection ceases altogether (this convective shutdown occurred by ∼10 days in preliminary simulations). To account for this moistening aloft in the simulations, an additional, constant moisture source is prescribed, which is objectively calculated as follows. A simulation is run with identical setup to CTL, though without a prescribed moisture source, which is hence characterized by drying with time. This drying tendency is averaged over the first 48 h, and reversed in sign. This now-positive moisture tendency is applied as the prescribed source. This prescribed source (28.9 W m^{-2} in the column integral) moistens the mid–upper troposphere, in addition to the moistening by clouds (64.0 W m^{-2}), to help offset the drying due to w_{wtg} subsidence (-107 W m^{-2}) (Fig. 4) (see Fig. 10a for context in the diurnal cycle). A sensitivity test carried out offline demonstrates no substantive impacts to removing the shallow near-surface drying of -0.75 g kg^{-1} (Fig. 4), which arises from the objective procedure through which this source is generated.

In each of the simulations, there is a very slight deepening of clouds and increase of rainfall with time (Fig. 5), despite the weak net drying tendency (Fig. 4). This subtle drift owes to a feedback between w_{wtg}, water vapor, and convective heating in the lower troposphere. This feedback, its sensitivity to the diurnal cycle, and its implications for

longer timescales are the subject of a separate study. The scope of this study is kept to the driving physics of the diurnal cycle within a given day, which is insensitive to this drift.

2.4. Diagnostic Quantities

Several diagnostic quantities are employed in this study to characterize the simulated moist convection. Two quantities are defined from microphysical variables to characterize clouds: cloud area coverage is the percentage of model columns containing cloud (defined as points where $q_c \geq 0.05$ g kg^{-1}, where q_c is cloud water mixing ratio); and cloud-top frequency is the occurrence of cloud top at each level divided by the total number of columns containing cloud, and multiplied by 100% (integration over z yields 100%).

The apparent heat source Q_1 and apparent moisture sink Q_2 [*Yanai et al.*, 1973] are calculated (in height coordinates) as

$$Q_1 \equiv \frac{\partial \overline{s}}{\partial t} + w_{wtg}\frac{\partial \overline{s}}{\partial z} = Q_R + L_v(\overline{c} - \overline{e}) - \frac{\partial}{\partial z}(\overline{s'w'}), \tag{1}$$

$$Q_2 \equiv -L_v\left(\frac{\partial \overline{q}}{\partial t} - \partial_t \overline{q}_{psc} + w_{wtg}\frac{\partial \overline{q}}{\partial z}\right) = L_v(\overline{c} - \overline{e}) + L_v\frac{\partial}{\partial z}(\overline{q'w'}), \tag{2}$$

where $s = c_pT + gz$ is dry static energy, Q_R is total radiative heating, L_v is the latent heat of vaporization, c is condensation, e is evaporation, w is the prognostic vertical motion (distinct from w_{wtg}), c_p is the specific heat of dry air at constant pressure, T is temperature, g is gravity, the subscript "psc" denotes the prescribed moisture tendency (section 2.3), the overbars denote horizontal averages, and the primes deviations from those averages. The horizontal eddy flux terms have been neglected [*Yanai and Johnson*, 1993]. Ice processes have also been neglected, but can be readily included [*Johnson et al.*, 2015]. Horizontal temperature advection is neglected, while horizontal moisture advection is replaced by

the prescribed source in (2). The convective heating, i.e., that due to net condensation and convergence of vertical eddy heat fluxes, is calculated from $Q_c = Q_1 - Q_R$.

The column-integrated moisture budget is calculated following *Yanai et al.* [1973] from

$$\left\langle \frac{\partial \overline{q}}{\partial t} \right\rangle = \langle \partial_t q_{psc} \rangle - \left\langle w_{wtg} \frac{\partial \overline{q}}{\partial z} \right\rangle - \langle Q_2 / L_v \rangle \,,$$
$$- \langle Q_2 / L_v \rangle = E_0 - P_0, \tag{3}$$

where the square brackets denote a mass-weighted integral over the depth of the troposphere, and domain-mean surface evaporation E_0 and precipitation P_0 are taken directly from the simulation output. The effect of water storage in clouds [*McNab and Betts*, 1978] was found to be negligible in these simulations, since for their duration the total cloud amount changes little (e.g., Fig. 5).

3. Results

3.1. Control simulation

The cloud population in CTL exhibits pronounced day-to-day persistence, both in cloud-top frequency and echo area coverage (see section 2.4 for definitions) (Fig. 5, top). There is, however, a subtle increase in cloud depth and rainfall with time (Fig. 5, bottom), as discussed in section 2.3. Cloud tops rarely exceed 4.5 km, despite appreciable CAPE and negligible convective inhibition (Fig. 2), implying the effectiveness with which subsidence drying by w_{wtg} impedes convective cloud deepening.

Two relatively distinct cloud populations are apparent, separated by a slight minimum in cloud-top frequency around 2 km. The very shallow clouds associated with peak frequency just above the mixed layer (dashed line) are "forced," in that they are tied to overshooting PBL eddies that do not achieve greater vertical development [*Stull*, 1985;

Esbensen, 1978]. Mixed-layer or PBL top is defined here as the level of minimum vertical eddy heat flux, which demarcates clear-air PBL eddies from cumulus-driven motions [*Betts*, 1975]. This forced population ascends slightly in the early afternoon as the mixed layer deepens each day (discussed in more detail later). The deeper cumuli associated with peak frequency centered around 3 km are "active," in that they have undergone buoyant growth well beyond mixed-layer top [*Stull*, 1985]. This active cloud population varies strongly as a function of the diurnal cycle, peaking in the late afternoon and dissipating through the overnight period.

Cloud area coverage depicts a minimum of ∼4.5% around 0800L each day, followed by an intriguing double peak of ∼8.5%. The first peak (just past noon) closely corresponds with the midday peak in SST (Fig. 5, bottom). This peak marks the beginning of light rainfall and the first appearance of deeper active cumuli, as indicated by increasing cloud-top frequency between 2 and 3 km. The second peak (1900L) closely coincides with the peak in rainfall and the frequency peak of the active clouds. The time-displacement of these two peaks in cloud area coverage suggests that there may be two distinct processes invigorating convection, with slightly differing phasing. Indeed, as will be shown, the diurnal cycle of SST and surface fluxes explains the midday cloud invigoration, whereas cloud-layer moistening driven largely by large-scale upward motion explains the later peak in clouds and rainfall (section 3.2).

Simulated rainfall is clearly tied to the activity of the deeper active clouds. It peaks around 1800∼1900L at 0.3∼0.5 mm day^{-1}, which is consistent in phasing with observations [*Sui et al.*, 1997] [RJ15]. Compared to suppressed regimes in DYNAMO, however, this simulated peak rainfall rate is weaker by a factor of ∼2 [RJ15]. This discrepancy is

consistent with stronger subsidence in CTL (especially in the lower troposphere) (Fig. 3). Although in observed suppressed regimes there is often an additional early-morning rainfall peak, which is not evident in CTL, *Sui et al.* [1997] demonstrate that this peak is associated with more organized, deeper cloud systems (i.e., in contrast to regimes of more "scattered rain cells"). It is plausible that the neglect of transient modes – i.e., diurnal tides [*Chapman and Lindzen*, 1970; *Woolnough et al.*, 2004] and equatorial waves [*Kiladis et al.*, 2009] – by virtue of the idealizations imposed, explains the lack of an early-morning rainfall peak. This issue requires further study.

Horizontal depictions of the cloud field through total cloud-liquid water path (i.e., q_c integrated over the column) reveal that the noontime cloud regime is scattered, while the overnight clouds appear to be fewer and more clustered (Figs. 6). The midday clouds are associated with small-scale open-cellular overturning motion, while the overnight clouds are tied to more extensive arcs of upward motion in connection with increased cold pool activity. The midday organization is fundamentally a Rayleigh–Bénard process, in that rainfall is of little influence, whereas nocturnally, the effect of rainfall-generated cold pools on the organization is evident (Fig. 5).

The evolution from small, non-raining cells around midday to larger, more cold-pool driven cloud organization later in the day is consistent with findings from DYNAMO radar observations [*Rowe and Houze*, 2015]. Modeling studies have also documented the afternoon increase in cold pool activity, and have argued for the importance of cold pools in amplifying overall convective activity [*Grabowski et al.*, 2006; *Khairoutdinov and Randall*, 2006; *Böing et al.*, 2012; *Li et al.*, 2014; *Schlemmer and Hohenegger*, 2014; *Feng et al.*, 2015]. Specifically, the organization of PBL moisture by cold pools can lead to

wider convective clouds, which are therefore less affected by dry-air entrainment and may grow deeper and produce greater rainfall than otherwise.

Despite more intense cold pools overnight in CTL, low-level wind speed peaks around midday (Fig. 7), as it does in corresponding DYNAMO observations (Fig. 1) [*Johnson et al.*, 2001; *Bellenger et al.*, 2010] [RJ15]. Daily-mean low-level wind speed increases from the base-state value of ∼1.5 m s^{-1} to 1.8 m s^{-1}, which is within 0.2 m s^{-1} of mean observed wind speed in the lowest 0.5 km in the corresponding R/V *Revelle* sounding (Fig. 2). Weak surface winds can also be noted during this period from the *Revelle* flux site [RJ15]. Domain-averaged surface latent and sensible heat flux (LH and SH, respectively) peaks at about the same time as wind speed, with diurnal variations of ∼30 and ∼5 W m^{-2}, respectively (Fig. 7). Although the mean magnitudes of the fluxes are quite consistent with those in the observations, the diurnal ranges are approximately half those in the corresponding DYNAMO observations (at least SP/MJO2; Fig. 1, right), since the daytime surface wind speed increase is substantially weaker in CTL than in DYNAMO [RJ15]. It is possible that this issue partly stems from the simplification imposed in the model framework through the use of constant surface exchange coefficients (section 2.1). Despite this diurnal amplitude bias, however, the role of diurnal SST and surface flux variation on midday convective invigoration can be readily isolated from the effects of direct radiative heating, as will be demonstrated later (section 3.2).

Diurnal mixed-layer deepening is well-captured in CTL, as depicted by the slight PBL deepening and ascent of the forced clouds early in each afternoon (Fig. 5, top). During suppressed regimes in COARE, mixed-layer top was observed to increase (in a composite-mean sense) from 502 m (0400L) to 574 m (1600L) in direct response to a large midday

increase of surface buoyancy flux [*Johnson et al.*, 2001]. Such diurnal cycles were not observed in disturbed COARE periods. In CTL, the mixed layer varies from 575 m (0630L) to 725 m (1500L). Therefore, although the mean depth and amplitude of the diurnal cycle are greater than observed, the phasing is in very good agreement.

Next, the diurnal evolution of diabatic processes is investigated to aid understanding of the diurnal evolution of clouds. w_{wtg} subsidence in the majority of the tropospheric column (in the daily-mean sense) is consistent with predominant radiative cooling (Figs. 3 and 8a,c). The diurnal cycle of Q_R is straightforward: the daytime increase of SW leads to a midday sign reversal of Q_R, with weak warming at midday. This daytime increase in Q_R, in turn, leads to relaxed w_{wtg} subsidence or weak ascent (i.e., from 4$\sim$6 km); however, the direct response of w_{wtg} to Q_R is highly modulated by moist convection within the cloud layer (i.e., up to $\sim$4 km).

The net impact of moist convection on the diabatic heating is conveyed by Q_c (Fig. 8b). (Although Q_1 is not shown, it can be inferred from the sum of Q_R and Q_c.) In the daily mean sense, Q_c exhibits warming in the PBL and lower cloud layer, and cooling in the upper cloud layer, which implies enhanced eddy heat flux convergence and net condensation, and eddy heat flux divergence and net evaporation, respectively. This Q_c signal explains reduced w_{wtg} subsidence (or weak ascent) in the lowest $\sim$2 km of the troposphere, and enhanced subsidence in the upper cloud layer (2$\sim$4 km).

The low-level Q_c warming exhibits two distinct peaks diurnally: one in the PBL around midday, and a later peak in the lower cloud layer (i.e., from 0.5$\sim$2 km between 1600 and 2000L). The midday peak is related to increased SST and surface fluxes (Figs. 5 and 7). As the PBL-rooted peak in Q_c warming transitions to the more elevated peak, the upper

cloud-layer signature of Q_c cooling ascends and amplifies. This amplified Q_c warming–cooling couplet reflects the late-afternoon deeper precipitating cloud population (Fig. 5). The afternoon upward shift of Q_c warming implies that this population of active cumuli are not as strongly rooted in the PBL, in contrast to the midday convection.

The midday combination of Q_R warming in the column and Q_c warming at low levels drives a highly nuanced response in w_{wtg}, which exhibits relaxed subsidence or weak ascent, with the strongest ascent in the lower cloud layer (0.5∼2 km) (recall the mode-dependency of the WTG relaxation, such that for shallower heating modes w_{wtg} responds more slowly; section 2.2). The midday signal of relaxed w_{wtg} subsidence (or weak ascent) precedes the transition in Q_c from PBL-rooted to more elevated heating associated with the late-afternoon convection. The combination of enhanced Q_c cooling in the upper cloud layer and increasing Q_R cooling in the midtroposphere amplifies w_{wtg} subsidence around 1800L, especially in the 2∼4-km layer. This subsidence begins to relax after each sunrise (0600L).

This diurnal cycle of w_{wtg} is consistent with that of large-scale vertical motion as observed in DYNAMO suppressed regimes, i.e., with enhanced subsidence nocturnally and reduced subsidence or weak ascent during the day [RJ15]. The amplitude of these diurnal variations, however, is greater in CTL (especially below 4 km) than that given by observations. In nature, the ITCZ, diurnal tides, or propagating 2-day waves likely influence the diurnal cycle of large-scale vertical motion, although such effects are not accounted for in this study [*Woolnough et al.*, 2004; *Haertel et al.*, 2008; *Johnson and Ciesielski*, 2013; *Zuluaga and Houze*, 2013].

Q_2 exhibits a regime change similar to Q_c, whereby apparent drying first peaks in the PBL (midday), and then shifts upwards into the lower cloud layer as moistening (and Q_c cooling) in the upper cloud layer amplifies and ascends (around ∼1600L) (Fig. 9a). The diurnal signal in q' (i.e., q with the 24-h running-mean signal subtracted) indicates that the apparent drying in the PBL around midday leads to net drying, despite maximum surface evaporation (Figs. 7 and 9b). According to (2), this midday drying must owe to the divergence of vertical eddy moisture fluxes, given that condensation does not occur below cloud base. The divergence of vertical eddy moisture fluxes can be interpreted in two ways: 1) the flux of anomalously moist parcels up and out of the mixed layer, and 2) the entrainment of dry parcels into the mixed layer. Both processes likely occur as the mixed layer deepens each day (Fig. 5) [*Johnson et al.*, 2001]. Prior studies have documented a nocturnal increase in mixed-layer humidity during field campaigns, though they could not explain this signal [*Sui et al.*, 1997; *Yasunaga et al.*, 2008]. The analysis here suggests that this diurnal moisture variation should be interpreted as the result of midday mixed-layer drying driven by vertical eddy fluxes as the mixed layer deepens.

The evening peak in Q_2 moistening centered at ∼3 km in the late afternoon exceeds ∼2.5 g kg^{-1}, which is consistent with values from sounding and lidar measurements during DYNAMO [*Bellenger et al.*, 2015] [RJ15]. This signature of late-afternoon convection, readily apparent both in Q_c and Q_2, roughly coincides with maximum values of q' and RH in the cloud layer (Figs. 8b and 9a,b). q' in the cloud layer exhibits dry conditions in the morning and moist conditions in the evening, with a magnitude change of 0.3∼0.6 g kg^{-1}. This q' signal is in close agreement with DYNAMO observations, both in phase and amplitude (Fig. 1). One wonders if this diurnal cycle in moisture owes to the convection

itself, rightfully so, although the phasing of Q_2 is telling: if convection were the sole cause of the midday moistening, Q_2 would be in quadrature with q', i.e., with maximum Q_2 moistening around midday. As becomes clear from the column-integrated moisture budget, w_{wtg} plays an important role in this moistening.

The column-integrated moisture budget indeed indicates that the diurnal cycle of w_{wtg} is of first-order importance in invigorating the net column moisture tendency, which peaks at ∼1400L (Fig. 10a). Although in the column-integrated sense advection by w_{wtg} is nearly always negative (consistent with predominant subsidence; Fig. 3), the daytime relaxation of subsidence, prompted by the midday increases in Q_R and Q_c, results in net moistening of the column (Fig. 8). The column moistening by convection is wrapped up into $E_0 - P_0$. Both E_0 and the constant prescribed moisture source act to persistently moisten the column. E_0 peaks shortly after 1200L in connection with the peak in SST (Fig. 7). Rainfall, although negligible in the sense of the column budget, peaks between 1800 and 2200L (Fig. 10b). This peak comes after SW warming has fully shut down, around the time of peak q' in the cloud-layer, and when the active cumuli are most active from the perspective of Q_c and Q_2 (Figs. 8a,b and 9).

In the next section, sensitivity tests are employed to further distinguish the two diurnal convective modes – that forced directly by SST and surface fluxes, and that by direct radiative heating. It will also be demonstrated that the diurnal modulation of w_{wtg} is largely controlled by the diurnal variation of direct radiative heating.

3.2. Sensitivity tests

The diurnal cloud field varies substantially among the sensitivity tests (Fig. 11). Relative to CTL, fixing SST to the diurnal mean (FIXSST) removes the midday peak in cloud

area coverage, leaving only the peak at ∼1800L associated with more abundant deeper clouds (Figs. 11a,b). This difference owes to a greatly reduced diurnal cycle in surface fluxes (Fig. 12). SH peaks around 0600L in FIXSST owing to the nocturnal decrease of low-level air temperature (not shown). Cloud-top frequency in the deeper late-afternoon cloud population is also slightly reduced in FIXSST. The diurnal cycle in mixed-layer depth is weaker, given the very small diurnal cycle of surface fluxes (although mixed-layer top is not plotted in Fig. 11, it can be directly inferred from elevation changes of the forced cumulus peak; Fig. 5). Doubling the diurnal SST amplitude (DBLSST), in contrast, emphasizes the midday peak in cloud-area coverage and the diurnal cycle in mixed-layer depth, since the diurnal cycle in surface fluxes is much larger, while also increasing cloud-top frequency in the deeper late-afternoon clouds (Figs. 11e and 12). The diurnal amplitude of surface fluxes in DBLSST is, in fact, closer to that observed in SP/MJO2 (Fig. 1, right) [RJ15].

Comparisons between CTL, FIXSST, and DBLSST imply that the diurnal cycle of SST and surface fluxes is critical to the midday peak in convection (i.e., the midday peak in cloud area coverage), but not to the deeper active cumulus population of the late afternoon, which persists in FIXSST. This suggests that the diurnal cycle of Q_R may be critical to the deeper afternoon clouds. The simulation with incoming SW fixed to the diurnal mean (FIXSW) supports this inference: the deeper late-afternoon cumulus peak is virtually absent, while the midday peak in cloud area coverage associated with diurnally varying SST and surface fluxes remains (Figs. 11c and 12). Clouds only reach ∼4 km in FIXSW, compared to ∼4.5 km in CTL and FIXSST. The diurnal cycle of mixed-layer depth is more impacted by the diurnal SST cycle, however. Mixed-layer depth varies

by 50 m in FIXSST, compared to 100 m in FIXSW, and 150 m in CTL. This suggests that surface fluxes are critical to the daytime increase in mixed-layer depth, while direct radiative heating plays a secondary role.

In NODC, convection exhibits no diurnal cycle, by design, and is consequently distributed evenly throughout the day (Figs. 11d and 12). Clouds remain shallower (up to ∼3.75 km) at all times in NODC than those in CTL and the other sensitivity tests, and rainfall is negligible, implying that the diurnal cycle yields daily-mean conditions that differ from those in the absence of the diurnal cycle.

The convective modes associated with diurnal cycles in SST and Q_R can be more clearly distinguished via vertical eddy buoyancy flux (Fig. 13), calculated from $c_p\overline{\rho}(\overline{w'\theta_v'})$, where ρ is the density of moist air and θ_v is virtual potential temperature. The midday peak in eddy buoyancy flux driven by the diurnal cycle of SST (present in CTL and FIXSW) is distinctly rooted in the PBL, with peaks in the PBL and centered at ∼1.25 km (Figs. 13a,c). In contrast, the late-afternoon peak in eddy flux associated with the more abundant deeper clouds (Fig. 5) has a distinctly elevated peak centered around 1.75 km, and is hence less rooted in the PBL (Figs. 13a,b). The midday mode is therefore referred to as the "forced mode," in that clouds therein result from forced eddies rooted in the PBL, while the deeper late-afternoon mode is called "active." CTL resembles a superposition of these two distinct diurnal convective modes, while NODC exhibits neither (Fig. 13d).

In XCLDRAD, the diurnal cycle of both clouds and surface fluxes is very similar to that in CTL (Figs. 11f and 12). There is slightly reduced frequency of deeper clouds in the late afternoon compared to CTL, however. This difference indicates the effect of clouds on direct radiative heating, which is discussed below in more detail.

Comparisons between CTL, FIXSST, and FIXSW indicate that the diurnal cycles in SST and Q_R are critical to the midday (shallower) forced cumulus mode and late-afternoon (deeper) active cumulus mode, respectively (Figs. 11a–c and 13). The midday mode can be explained by the diurnal cycle of surface fluxes, which drives a midday increase in buoyancy-driven PBL overturning, deepening of the mixed layer, and reduction of convective inhibition [*Stull*, 1985; *Johnson et al.*, 2001; *Bellenger et al.*, 2010].

The late-afternoon mode is more complex, given that neither the diurnal cycle in Q_R nor that in SST, which both peak at midday, can directly drive late-afternoon cloud invigoration. The response of w_{wtg} to the diurnal cycle of diabatic heating, however, can affect the convection. The importance of the diurnal cycle in w_{wtg} to the diurnal modulation of cloud-layer humidity has been demonstrated in section 3.1 (Figs. 8c, 9b, and 10a). Comparison among the sensitivity tests of vertical moisture advection by w_{wtg} indeed reveals vast differences, as a function of the diurnal cycle of Q_R (Fig. 14, top). In CTL, FIXSST, DBLSST, and XCLDRAD, Q_R has a regular diurnal cycle, and there is a large variation of this advection term. Each of these simulations exhibits the late-day deeper convective mode (Figs. 11 and 13). In NODC and FIXSW, however, the diurnal variation of w_{wtg} advection is minimal, and the deeper late-afternoon mode is absent.

The diurnal signal of q' in the sensitivity tests corroborates that the diurnal variation of w_{wtg}, and hence Q_R, is critical to the diurnal variation of cloud-layer humidity (Fig. 15). In the simulations in which Q_R is fixed, there is very little q' variation above the PBL. The diurnal cycle in SST slightly augments this daytime cloud-layer moistening, however, as highlighted by differences between CTL and DBLSST, and between CTL and FIXSST. In DBLSST, for example, q' exhibits a higher-amplitude diurnal cycle in the cloud layer.

DBLSST is also characterized by a greater variation of moisture in the PBL, i.e., greater midday drying, than in CTL. Greater midday PBL drying is consistent with more vigorous eddy exchange between the PBL and overlying free troposphere, as a result of higher-amplitude surface flux variation and greater afternoon mixed-layer deepening (Fig. 11e and 12.

Comparison between the sensitivity tests also demonstrates that evening rainfall is highly dependent on the daytime cloud-layer moistening, and is therefore virtually absent in FIXSW and NODC (Fig. 14, bottom). Intriguingly, rainfall is also negligible in XCLDRAD, despite comparable diurnal moistening to that in CTL (Figs. 15a,f). The deviation of LW and SW heating in cloudy columns (i.e., those where $q_c \geq 0.05$ g kg^{-1}) from the total domain-averaged tendencies reveals the effect of direct cloud–radiation interaction in CTL (Fig. 16). While the net effect of clouds on SW is minimal, the impact on LW is substantial. In cloudy columns, longwave cooling is enhanced in the upper cloud layer, and reduced in the PBL and lower cloud layer (a similar feedback is critical to thin, high clouds; *Webster and Stephens* [1980]). This LW effect, which locally invigorates convection, is strongest in the deeper late-afternoon clouds. Without this local LW effect (i.e., in XCLDRAD), clouds are slightly less vigorous, and rainfall is hence negligible (Figs. 11f and 14).

Given that this cloud–radiative effect is predominately in LW, it is fundamentally non-diurnal. *Xu and Randall* [1995] argued that, in deep-convective regimes, SW heating leads to local stabilization of cloudy areas during the day, which hence suppresses daytime rainfall. Although the SW feedback in CTL is consistent with this argument, the magnitude of this effect indicates that it is less important in this shallow cloud regime (Fig. 16,

bottom). Instead, the diurnal feedback between SW heating and large-scale circulation is critical to the diurnal evolution of clouds (Fig. 11).

4. Summary and Conclusions

An idealized model experiment has been executed to study the pronounced diurnal cycle of shallow moist convection as observed in suppressed regimes in the tropical oceanic warm pool regions [*Sui et al.*, 1997; *Johnson et al.*, 2001; *Bellenger et al.*, 2010] [RJ15]. In such regimes, the diurnal cycles of shortwave heating and SST are at maximum amplitude, and convective clouds exhibit prominent daytime invigoration coinciding with moistening of the low–midtroposphere (Fig. 1) [RJ15]. This study has attempted to discern the governing processes in this diurnal cycle, and to assess the relative roles of diurnally varying SST and direct radiative heating therein.

The experiment was carried out with CM1 [*Bryan and Fritsch*, 2002] discretized at cloud-resolving scales (i.e., $\Delta x = \Delta y = 200$ m; and $\Delta z = 50$ m in the lower troposphere). The diurnal cycle in each (sixteen-day) simulation was forced by a homogeneously prescribed repeating diurnal cycle of SST (with interactive surface fluxes) and diurnally varying, fully interactive radiation. The base-state sounding (Fig. 2) and prescribed SST diurnal cycle (Fig. 5) were taken from measurements from a DYNAMO suppressed phase.

To represent large-scale vertical motion and account for subsidence drying, the spectral weak temperature gradient (WTG) scheme of *Herman and Raymond* [2014] was invoked in CM1. In this scheme, the large-scale vertical motion (w_{wtg}) required to offset simulated diabatic heating via adiabatic motion is diagnosed (in a relaxed manner), and then used to advect temperature and moisture. Therefore, w_{wtg} responds to diurnal changes in the diabatic heating, e.g., with reduced subsidence during the day in response to shortwave

warming. The diurnal variation of w_{wtg} was found to be consistent with the diurnal variation of large-scale vertical motion during DYNAMO suppressed periods, although with slightly greater simulated amplitude than that given by observations (specifically, below 4 km) [RJ15].

The observed daytime cumulus invigoration was well-replicated in a control simulation, wherein cloud tops predominately grow from between 0.5∼1.5 km around midday to ∼3 km by the late afternoon, and decay overnight (Figs. 1 and 5). Very light rainfall coincides with the deeper late-afternoon clouds (Fig. 5). The daytime moistening of the low–midtroposphere was also well replicated by CTL (with moist conditions in the afternoon), both in phase and amplitude (Fig. 9b). Although a distinct, secondary nocturnal peak in convection is sometimes present in suppressed regimes in nature, this peak likely owes to propagating modes (e.g., diurnal tides or two-day waves), which are not accounted for in this study [*Sui et al.*, 1997; *Woolnough et al.*, 2004; *Haertel et al.*, 2008; *Zuluaga and Houze*, 2013] [RJ15].

The findings of this study indicate that SST and direct radiative heating invigorate convection in distinct manners. These two modes of cumulus invigoration are distinguished (respectively) as follows: a midday "forced" mode, characterized by clouds with tops generally below 2 km and very little rainfall; and a late-afternoon "active" mode associated with more abundant deeper clouds and greater rainfall. These two modes are depicted schematically via vertical eddy buoyancy flux in Fig. 17a, with the salient features of each mode shown in Figs. 17b,c. The midday forced mode is strongly rooted within the PBL, attesting to its fundamental link to SST and surface fluxes. The deeper active mode, in turn, is associated with enhanced humidity within the cloud layer, and is less rooted in

the PBL. Cloud-layer humidity increases during the day in response to relaxed w_{wtg} subsidence, which is primarily driven by the daytime increase of shortwave heating. Thus, the deeper active mode fundamentally owes to the diurnal cycle of large-scale vertical motion, which in this model framework is driven by the diurnal cycle of direct radiative heating. Making clouds transparent to radiation has little effect on the domain-averaged budgets and general evolution of clouds; however, this removes the local cloud–longwave feedback [*Webster and Stephens*, 1980], making convection slightly weaker, and rainfall negligible.

Systematic changes in mesoscale PBL circulation manifest in the diurnal cycle. The midday forced mode is manifest in Rayleigh–Bénard cellular convection, wherein precipitation processes likely have little influence (Figs. 17b). In the active mode, precipitation leads to cold pools, the spreading of which lead to wider cellular structures (Fig. 17c), consistent with DYNAMO observations [*Rowe and Houze*, 2015]. Modeling studies have shown that such cold pool activity can amplify the convection [*Grabowski et al.*, 2006; *Khairoutdinov and Randall*, 2006; *Böing et al.*, 2012; *Li et al.*, 2014; *Schlemmer and Hohenegger*, 2014; *Feng et al.*, 2015]. Specifically, the organization of PBL moisture by cold pools can lead to wider convective clouds, which are therefore less affected by dry-air entrainment, and may grow deeper and produce greater rainfall than otherwise. The feedback from cold pools in the diurnal cycle has not been isolated here, however.

The diurnal variation of SST and surface fluxes was found to be critical to daytime mixed-layer deepening and drying, while direct radiative warming in the PBL plays a secondary role in this process. The midday drying of the PBL is due to the divergence of eddy moisture flux as the mixed layer deepens. Prior studies have documented a nocturnal increase in mixed-layer humidity, and could not explain this signal [*Sui et al.*,

1997; *Yasunaga et al.*, 2008]. The findings of this study suggest that this diurnal moisture variation should be interpreted as the result of midday mixed-layer drying.

An important caveat of this study is the that the diurnal amplitude of surface fluxes was underrepresented by the model. This may owe to the assumption of constant surface heat exchange coefficients. It is therefore possible that the relative role of diurnally varying surface fluxes on the convection is underrepresented (Figs. 1 and 7). Comparison between the control simulation and DBLSST, a simulation in which the diurnal amplitude of SST is doubled, indicates that greater diurnal flux variation indeed bolsters the late-afternoon active convective mode, while also amplifying mixed-layer variability.

More work is ultimately required to better understand the diurnal cycle of tropical convection and its interaction with large-scale circulation. Observations fail to fully depict this diurnal cycle, and particularly that in large-scale circulation. Future field experiments with high-frequency, vertically-resolved observations might yield important steps forward in this regard.

That the cumulus diurnal cycle is a fundamentally nonlinear process has been exemplified in this study. For example, without the diurnal cycle, rainfall is negligible, and clouds remain shallower at all times. Given this nonlinearity, it is likely that improving our understanding of the diurnal cycle and the scale interactions that manifest therein will ultimately lead to improved understanding of cloud–climate feedbacks in general [*Bony et al.*, 2015].

Acknowledgments. This study greatly benefited from the comments of Dave Randall, Eric Maloney, Sue van dan Heever, and V. Chandrasekar (Colorado State University); David Raymond and Michael Herman (New Mexico Tech.); and Hugh Morrison

(NCAR). George Bryan (NCAR) is also acknowledged for his tireless work on CM1, and for his assistance in resolving modeling issues along the course of this research. The comments from two anonymous reviewers substantially helped to improve the clarity of this study. All model data described in this study resides on the NCAR Yellowstone system, and is available for community use. This research has been funded by National Science Foundation grants AGS–1138353 and AGS–1360237. JHR is currently supported by the Alexander von Humboldt Foundation.

References

Bellenger, H., Y. N. Takayabu, T. Ushiyama, and K. Yoneyama (2010), Role of diurnal warm layers in the diurnal cycle of convection over the tropical Indian Ocean during MISMO, *Monthly Weather Review*, *138*(6), 2426–2433, doi:10.1175/2010MWR3249.1.

Bellenger, H., K. Yoneyama, M. Katsumata, T. Nishizawa, K. Yasunaga, and R. Shirooka (2015), Observation of Moisture Tendencies Related to Shallow Convection, *Journal of the Atmospheric Sciences*, *72*, 641–659, doi:10.1175/JAS-D-14-0042.1.

Bernie, D. J., S. J. Woolnough, J. M. Slingo, and E. Guilyardi (2005), Modeling diurnal and intraseasonal variability of the ocean mixed layer., *Journal of Climate...*, *18*(1997), 1190–1202.

Betts, A. K. (1975), Parametric Interpretation of Trade-Wind Cumulus Budget Studies, doi:10.1175/1520-0469(1975)032¡1934:PIOTWC¿2.0.CO;2.

Böing, S. J., H. J. J. Jonker, a. P. Siebesma, and W. W. Grabowski (2012), Influence of the Subcloud Layer on the Development of a Deep Convective Ensemble, *Journal of the Atmospheric Sciences*, *69*(9), 2682–2698, doi:10.1175/JAS-D-11-0317.1.

Bony, S., B. Stevens, D. M. W. Frierson, C. Jakob, M. Kageyama, R. Pincus, T. G. Shepherd, S. C. Sherwood, A. P. Siebesma, A. H. Sobel, M. Watanabe, and M. J. Webb (2015), Clouds, circulation and climate sensitivity, *Nature Geoscience*, *8*(4), 261–268, doi:10.1038/ngeo2398.

Bryan, G., and J. Fritsch (2002), A benchmark simulation for moist nonhydrostatic numerical models, *Monthly weather review*, (1992), 2917–2928.

Bryan, G. H., J. C. Wyngaard, and J. M. Fritsch (2003), Resolution Requirements for the Simulation of Deep Moist Convection, *Monthly Weather Review*, *131*(10), 2394–2416,

doi:10.1175/1520-0493(2003)131¡2394:RRFTSO¿2.0.CO;2.

Chapman, S., and R. S. Lindzen (1970), *Atmospheric Tides*, 200 pp., D. Reidel Press, Dordrecht, Holland.

Charney, J. G. (1963), A note on large-scale motions in the tropics, *Journal of the Atmospheric Sciences*, *20*(6), 607–609, doi:10.1175/1520-0469(1963)020¡0607:ANOLSM¿2.0.CO;2.

Chen, S. S., and R. A. Houze (1997), Diurnal variation and life-cycle of deep convective systems over the tropical pacific warm pool, *Quarterly Journal of the Royal Meteorological Society*, *123*(538), 357–388, doi:10.1002/qj.49712353806.

Chou, M.-D., and M. J. Suarez (1994), An efficient thermal infrared radiation parameterization for use in general circulation models, *NASA Tech. Memo. 104606*, *vol. 3*, 102 pp.

Chou, M.-D., and M. J. Suarez (1999), A solar radiation parameterization for atmospheric studies, *NASA Tech. Memo., NASA/TM-1999-104606*, *15*.

Clayson, C. A., and A. S. Bogdanoff (2013), The Effect of Diurnal Sea Surface Temperature Warming on Climatological Air–Sea Fluxes, *Journal of Climate*, *26*(8), 2546–2556, doi:10.1175/JCLI-D-12-00062.1.

Dai, A. (2001), Global precipitation and thunderstorm frequencies. Part II: Diurnal variations, *Journal of Climate*, *14*, 1112–1128, doi:10.1175/1520-0442(2001)014¡1112:GPATFP¿2.0.CO;2.

Dai, A., and C. Deser (1999), Diurnal and semidiurnal variations in global surface wind and divergence fields, *Journal of Geophysical Research*, *104*(D24), 31,109, doi:10.1029/1999JD900927.

Deardorff, J. W. (1980), Stratocumulus-capped mixed layers derived from a three-dimensional model, *Boundary-Layer Meteorology*, *18*(4), 495–527, doi: 10.1007/BF00119502.

Dunion, J. P., C. D. Thorncroft, and C. S. Velden (2014), The Tropical Cyclone Diurnal Cycle of Mature Hurricanes, *Monthly Weather Review*, *142*(10), 3900–3919, doi: 10.1175/MWR-D-13-00191.1.

Esbensen, S. (1978), Bulk Thermodynamic Effects and Properties of Small Tropical Cumuli, *Journal of the Atmospheric Sciences*, *35*(5), 826–837, doi:10.1175/1520-0469(1978)035¡0826:BTEAPO¿2.0.CO;2.

Fairall, C. W., E. F. Bradley, J. S. Godfrey, G. A. Wick, J. B. Edson, and G. S. Young (1996), Cool-skin and warm-layer effects on sea surface temperature, *Journal of Geophysical Research*, *101*, 1295–1308.

Feng, Z., S. Hagos, A. K. Rowe, C. D. Burleyson, M. N. Martini, and S. P. de Szoeke (2015), Mechanisms of convective cloud organization by cold pools over tropical warm ocean during the AMIE/DYNAMO field campaign, *Journal of Advances in Modeling Earth Systems*, *7*(2), 357–381, doi:10.1002/2014MS000384.

Gille, S. T., S. G. Llewellyn Smith, and S. M. Lee (2003), Measuring the sea breeze from QuikSCAT Scatterometry, *Geophysical Research Letters*, *30*(3), 1114, doi: 10.1029/2002GL016230.

Grabowski, W. W., P. Bechtold, A. Cheng, R. Forbes, C. Halliwell, M. Khairoutdinov, S. Lang, T. Nasuno, J. Petch, W.-K. Tao, R. Wong, X. Wu, and K.-M. Xu (2006), Daytime convective development over land: A model intercomparison based on LBA observations, *Quarterly Journal of the Royal Meteorological Society*, *132*(615), 317–344,

doi:10.1256/qj.04.147.

Gray, W. M., and R. W. Jacobson (1977), Diurnal variation of deep cumulus convection, *Monthly Weather Review*, *105*, 1171–1188.

Haertel, P. T., G. N. Kiladis, A. Denno, and T. M. Rickenbach (2008), Vertical-mode decompositions of 2-day waves and the Madden–Julian Oscillation, *Journal of the Atmospheric Sciences*, *65*(3), 813–833, doi:10.1175/2007JAS2314.1.

Halpern, D., and R. K. Reed (1976), Heat budget of the upper ocean under light winds, *Journal of Physical Oceanography*, *6*(6), 972–975, doi:10.1175/1520-0485(1976)006¡0972:HBOTUO¿2.0.CO;2.

Herman, M. J., and D. J. Raymond (2014), WTG cloud modeling with spectral decomposition of heating, *Journal of Advances in Modeling Earth Systems*, *6*, 1121–1140, doi:10.1002/2014MS000359.

Johnson, R. H., and P. E. Ciesielski (2013), Structure and properties of Madden–Julian Oscillations deduced from DYNAMO sounding arrays, *Journal of the Atmospheric Sciences*, *70*(10), 3157–3179, doi:10.1175/JAS-D-13-065.1.

Johnson, R. H., and X. Lin (1997), Episodic Trade Wind Regimes over the Western Pacific Warm Pool, *Journal of the Atmospheric Sciences*, *54*(15), 2020–2034, doi:10.1175/1520-0469(1997)054¡2020:ETWROT¿2.0.CO;2.

Johnson, R. H., P. E. Ciesielski, and J. A. Cotturone (2001), Multiscale Variability of the Atmospheric Mixed Layer over the Western Pacific Warm Pool, *Journal of the Atmospheric Sciences*, *58*(18), 2729–2750, doi:10.1175/1520-0469(2001)058¡2729:MVOTAM¿2.0.CO;2.

Johnson, R. H., P. E. Ciesielski, J. H. Ruppert, and M. Katsumata (2015), Sounding-Based Thermodynamic Budgets for DYNAMO, *Journal of the Atmospheric Sciences*, *72*(2), 598–622, doi:10.1175/JAS-D-14-0202.1.

Khairoutdinov, M., and D. Randall (2006), High-Resolution Simulation of Shallow-to-Deep Convection Transition over Land, *Journal of the Atmospheric Sciences*, *63*(12), 3421–3436, doi:10.1175/JAS3810.1.

Kiladis, G. N., M. C. Wheeler, P. T. Haertel, K. H. Straub, and P. E. Roundy (2009), Convectively coupled equatorial waves, *Reviews of Geophysics*, *47*(2), RG2003, doi:10.1029/2008RG000266.

Klemp, J. B., W. C. Skamarock, and J. Dudhia (2007), Conservative Split-Explicit Time Integration Methods for the Compressible Nonhydrostatic Equations, doi:10.1175/MWR3440.1.

Kogan, Y. (2013), A Cumulus Cloud Microphysics Parameterization for Cloud-Resolving Models, *Journal of the Atmospheric Sciences*, *70*(5), 1423–1436, doi:10.1175/JAS-D-12-0183.1.

Li, Z., P. Zuidema, and P. Zhu (2014), Simulated Convective Invigoration Processes at Trade Wind Cumulus Cold Pool Boundaries, *Journal of the Atmospheric Sciences*, *71*(8), 2823–2841, doi:10.1175/JAS-D-13-0184.1.

Li, Z., P. Zuidema, P. Zhu, and H. Morrison (2015), The Sensitivity of Simulated Shallow Cumulus Convection and Cold Pools to Microphysics, *Journal of the Atmospheric Sciences*, *72*(9), 3340–3355, doi:10.1175/JAS-D-14-0099.1.

Liu, C., and M. W. Moncrieff (1998), A Numerical Study of the Diurnal Cycle of Tropical Oceanic Convection, *Journal of the Atmospheric Sciences*, *55*(13), 2329–2344, doi:

10.1175/1520-0469(1998)055¡2329:ANSOTD¿2.0.CO;2.

Madden, R., and P. Julian (1972), Description of global-scale circulation cells in the tropics with a 40-50 day period, *Journal of the Atmospheric Sciences*, *29*, 1109–1123.

Madden, R. A., and P. R. Julian (1971), Detection of a 40-50 day oscillation in the zonal wind in the tropical Pacific, *Journal of the Atmospheric Sciences*, *28*, 702–708.

Mapes, B. E. (1993), Gregarious Tropical Convection, doi:10.1175/1520-0469(1993)050¡2026:GTC¿2.0.CO;2.

Mapes, B. E. (2001), Water's two height scales: The moist adiabat and the radiative troposphere, *Quarterly Journal of the Royal Meteorological Society*, *127*(577), 2353–2366, doi:10.1002/qj.49712757708.

Mapes, B. E., and R. a. Houze (1993), Cloud Clusters and Superclusters over the Oceanic Warm Pool, *Monthly Weather Review*, *121*(5), 1398–1416, doi:10.1175/1520-0493(1993)121¡1398:CCASOT¿2.0.CO;2.

Mapes, B. E., and R. A. Houze (1995), Diabatic Divergence Profiles in Western Pacific Mesoscale Convective Systems, *Journal of the Atmospheric Sciences*, *52*(10), 1807–1828, doi:10.1175/1520-0469(1995)052¡1807:DDPIWP¿2.0.CO;2.

Matthews, A. J., D. B. Baranowski, K. J. Heywood, P. J. Flatau, and S. Schmidtko (2014), The Surface Diurnal Warm Layer in the Indian Ocean during CINDY/DYNAMO, *Journal of Climate*, *27*(24), 9101–9122, doi:10.1175/JCLI-D-14-00222.1.

McNab, A. L., and A. K. Betts (1978), A mesoscale budget study of cumulus convection, *Monthly Weather Review*, *106*(9), 1317–1331, doi:10.1175/1520-0493(1978)106¡1317:AMBSOC¿2.0.CO;2.

Melhauser, C., and F. Zhang (2014), Diurnal Radiation Cycle Impact on the Pregenesis Environment of Hurricane Karl (2010), *Journal of the Atmospheric Sciences*, *71*(4), 1241–1259, doi:10.1175/JAS-D-13-0116.1.

Morrison, H., J. A. Curry, and V. I. Khvorostyanov (2005), A New Double-Moment Microphysics Parameterization for Application in Cloud and Climate Models. Part I: Description, *Journal of the Atmospheric Sciences*, *62*(6), 1665–1677, doi:10.1175/JAS3446.1.

Morrison, H., G. Thompson, and V. Tatarskii (2009), Impact of Cloud Microphysics on the Development of Trailing Stratiform Precipitation in a Simulated Squall Line: Comparison of One- and Two-Moment Schemes, *Monthly Weather Review*, *137*(3), 991–1007, doi:10.1175/2008MWR2556.1.

Moum, J. N., S. P. D. Szoeke, W. D. Smyth, J. B. Edson, H. L. DeWitt, A. J. Moulin, E. J. Thompson, C. J. Zappa, S. a. Rutledge, R. H. Johnson, and C. W. Fairall (2013), Air-sea interactions from westerly wind bursts during the November 2011 MJO in the Indian Ocean, *Bulletin of the American Meteorological Society 2013 ; e-View*, (November 2013), 1–49, doi:http://dx.doi.org/10.1175/BAMS-D-12-00225.1.

Nicholls, M. E. (2015), An investigation of how radiation may cause accelerated rates of tropical cyclogenesis and diurnal cycles of convective activity, *Atmospheric Chemistry and Physics Discussions*, *15*(5), 6125–6205, doi:10.5194/acpd-15-6125-2015.

Nicholls, M. E., R. A. Pielke, and W. R. Cotton (1991), Thermally Forced Gravity Waves in an Atmosphere at Rest, *Journal of the Atmospheric Sciences*, *48*(16), 1869–1884, doi:10.1175/1520-0469(1991)048¡1869:TFGWIA¿2.0.CO;2.

Nitta, T., and S. Esbensen (1974), Heat and moisture budget analyses using BOMEX data, *Monthly Weather Review*, *102*(1), 17–28, doi:10.1175/1520-

0493(1974)102¡0017:HAMBAU¿2.0.CO;2.

Price, J. F., R. a. Weller, and R. Pinkel (1986), Diurnal cycling: Observations and models of the upper ocean response to diurnal heating, cooling, and wind mixing, *Journal of Geophysical Research*, *91*(C7), 8411, doi:10.1029/JC091iC07p08411.

Randall, D. A., Harshvardhan, and D. A. Dazlich (1991), Diurnal Variability of the Hydrologic Cycle in a General Circulation Model, *Journal of the Atmospheric Sciences*, *48*(1), 40–62, doi:10.1175/1520-0469(1991)048¡0040:DVOTHC¿2.0.CO;2.

Raymond, D. J., and X. Zeng (2005), Modelling tropical atmospheric convection in the context of the weak temperature gradient approximation, *Quarterly Journal of the Royal Meteorological Society*, *131*(608), 1301–1320, doi:10.1256/qj.03.97.

Rowe, A. K., and R. A. Houze (2015), Cloud organization and growth during the transition from suppressed to active MJO conditions, *Journal of Geophysical Research: Atmospheres*, pp. n/a–n/a, doi:10.1002/2014JD022948.

Ruppert, J. H., and R. H. Johnson (2015), Diurnally Modulated Cumulus Moistening in the Preonset Stage of the Madden–Julian Oscillation during DYNAMO*, *Journal of the Atmospheric Sciences*, *72*(4), 1622–1647, doi:10.1175/JAS-D-14-0218.1.

Schlemmer, L., and C. Hohenegger (2014), The formation of wider and deeper clouds as a result of cold-pool dynamics., *Journal of the Atmospheric Sciences*, p. 140421141808009, doi:10.1175/JAS-D-13-0170.1.

Sentić, S., S. L. Sessions, and Ž. Fuchs (2015), Diagnosing DYNAMO convection with weak temperature gradient simulations, *Journal of Advances in Modeling Earth Systems*, *7*(4), 1849–1871, doi:10.1002/2015MS000531.

Shinoda, T. (2005), Impact of the Diurnal Cycle of Solar Radiation on Intraseasonal SST Variability in the Western Equatorial Pacific, *Journal of Climate*, *18*(14), 2628–2636, doi:10.1175/JCLI3432.1.

Sobel, A., S. Wang, and D. Kim (2014), Moist Static Energy Budget of the MJO during DYNAMO, *Journal of the Atmospheric Sciences*, *71*(11), 4276–4291, doi:10.1175/JAS-D-14-0052.1.

Sobel, a. H., and C. S. Bretherton (2000), Modeling tropical precipitation in a single column, *Journal of Climate*, *13*, 4378–4392, doi:10.1175/1520-0442(2000)013¡4378:MTPIAS¿2.0.CO;2.

Sobel, A. H., J. Nilsson, and L. M. Polvani (2001), The Weak Temperature Gradient Approximation and Balanced Tropical Moisture Waves*, *Journal of the Atmospheric Sciences*, *58*(23), 3650–3665, doi:10.1175/1520-0469(2001)058¡3650:TWTGAA¿2.0.CO;2.

Soloviev, A., and R. Lukas (1997), Observation of large diurnal warming events in the near-surface layer of the western equatorial Pacific warm pool, *Deep Sea Research Part I: Oceanographic Research Papers*, *44*(6), 1055–1076, doi:10.1016/S0967-0637(96)00124-0.

Stevens, B., and A. Seifert (2008), Understanding macrophysical outcomes of microphysical choices in simulations of shallow cumulus convection, *Journal of the Meteorological Society of Japan*, *86A*(August 2006), 143–162, doi:10.2151/jmsj.86A.143.

Stramma, L., P. Cornillon, R. A. Weller, J. F. Price, and M. G. Briscoe (1986), Large diurnal sea surface temperature variability: Satellite and in situ measurements, *Journal of Physical Oceanography*, *16*(5), 827–837, doi:10.1175/1520-0485(1986)016¡0827:LDSSTV¿2.0.CO;2.

Stull, R. B. (1985), A Fair-Weather Cumulus Cloud Classification Scheme for Mixed-Layer Studies, *Journal of Climate and Applied Meteorology*, *24*(1), 49–56, doi:10.1175/1520-0450(1985)024¡0049:AFWCCC¿2.0.CO;2.

Sui, C.-H., K.-M. Lau, Y. N. Takayabu, and D. A. Short (1997), Diurnal variations in tropical oceanic cumulus convection during TOGA COARE, *Journal of the Atmospheric Sciences*, *54*(1990), 639–655.

Takemi, T., O. Hirayama, and C. Liu (2004), Factors responsible for the vertical development of tropical oceanic cumulus convection, *Geophysical Research Letters*, *31*(L11109), 4, doi:10.1029/2004GL020225.

Tao, W.-K., S. Lang, J. Simpson, C.-H. Sui, B. Ferrier, and M.-D. Chou (1996), Mechanisms of Cloud-Radiation Interaction in the Tropics and Midlatitudes, doi:10.1175/1520-0469(1996)053¡2624:MOCRII¿2.0.CO;2.

VanZanten, M. C., B. Stevens, L. Nuijens, a. P. Siebesma, a. S. Ackerman, F. Burnet, a. Cheng, F. Couvreux, H. Jiang, M. Khairoutdinov, Y. Kogan, D. C. Lewellen, D. Mechem, K. Nakamura, a. Noda, B. J. Shipway, J. Slawinska, S. Wang, and a. Wyszogrodzki (2011), Controls on precipitation and cloudiness in simulations of trade-wind cumulus as observed during RICO, *Journal of Advances in Modeling Earth Systems*, *3*(6), M06,001, doi:10.1029/2011MS000056.

Webster, P. J., and G. L. Stephens (1980), Tropical Upper-Tropospheric Extended Clouds: Inferences from Winter MONEX, *Journal of the Atmospheric Sciences*, *37*(7), 1521–1541, doi:10.1175/1520-0469-37.7.1521.

Webster, P. J., C. A. Clayson, and J. A. Curry (1996), Clouds, Radiation, and the Diurnal Cycle of Sea Surface Temperature in the Tropical Western Pacific, *Journal of Climate*,

9(8), 1712–1730, doi:10.1175/1520-0442(1996)009¡1712:CRATDC¿2.0.CO;2.

Weller, R. A., and S. P. Anderson (1996), Surface meteorology and air-sea fluxes in the western equatorial Pacific warm pool during the TOGA Coupled Ocean-Atmosphere Response Experiment, *Journal of Climate*, *9*(8), 1959–1990, doi:10.1175/1520-0442(1996)009¡1959:SMAASF¿2.0.CO;2.

Wicker, L. J., and W. C. Skamarock (2002), Time-Splitting Methods for Elastic Models Using Forward Time Schemes, *Monthly Weather Review*, *130*(8), 2088–2097, doi:10.1175/1520-0493(2002)130¡2088:TSMFEM¿2.0.CO;2.

Wilhelmson, R. B., and C.-S. Chen (1982), A Simulation of the Development of Successive Cells Along a Cold Outflow Boundary, *Journal of the Atmospheric Sciences*, *39*(7), 1466–1483, doi:10.1175/1520-0469(1982)039¡1466:ASOTDO¿2.0.CO;2.

Woolnough, S. J., J. M. Slingo, and B. J. Hoskins (2004), The Diurnal Cycle of Convection and Atmospheric Tides in an Aquaplanet GCM, doi:10.1175/JAS3290.1.

Xu, K.-M., and D. A. Randall (1995), Impact of Interactive Radiative Transfer on the Macroscopic Behavior of Cumulus Ensembles. Part II: Mechanisms for Cloud-Radiation Interactions, *Journal of the Atmospheric Sciences*, *52*(7), 800–817, doi:10.1175/1520-0469(1995)052¡0800:IOIRTO¿2.0.CO;2.

Yanai, M., and R. H. Johnson (1993), Impacts of cumulus convection on thermodynamic fields, in *Meteor. Monographs*, vol. 24, chap. 4, pp. 39–62.

Yanai, M., S. Esbensen, and J.-H. Chu (1973), Determination of bulk properties of tropical cloud clusters from large-scale heat and moisture budgets, *Journal of the Atmospheric Sciences*, *30*(4), 611–627, doi:10.1175/1520-0469(1973)030¡0611:DOBPOT¿2.0.CO;2.

Yang, G.-Y., and J. Slingo (2001), The Diurnal Cycle in the Tropics, *Monthly Weather Review*, *129*(4), 784–801, doi:10.1175/1520-0493(2001)129¡0784:TDCITT¿2.0.CO;2.

Yang, S., and E. A. Smith (2006), Mechanisms for Diurnal Variability of Global Tropical Rainfall Observed from TRMM, *Journal of Climate*, *19*(20), 5190–5226, doi: 10.1175/JCLI3883.1.

Yano, J.-I., and M. Bonazzola (2009), Scale Analysis for Large-Scale Tropical Atmospheric Dynamics, *Journal of the Atmospheric Sciences*, *66*(1), 159–172, doi: 10.1175/2008JAS2687.1.

Yasunaga, K., M. Fujita, T. Ushiyama, K. Yoneyama, Y. N. Takayabu, and M. Yoshizaki (2008), Diurnal variations in precipitable water observed by shipborne GPS over the tropical Indian Ocean, *SOLA*, *4*, 97–100.

Zuluaga, M. D., and R. A. Houze (2013), Evolution of the Population of Precipitating Convective Systems over the Equatorial Indian Ocean in Active Phases of the Madden–Julian Oscillation, *Journal of the Atmospheric Sciences*, *70*(9), 2713–2725, doi:10.1175/JAS-D-12-0311.1.

Figure 1. Composite diurnal cycle of shallow moist convection during the (left) Oct and (right) Nov MJO suppressed periods of the DYNAMO field experiment (Dynamics of the Madden–Julian Oscillation). (top) Water vapor mixing ratio q with the daily-mean removed (q'; every 10^{-1} g kg^{-1}); (middle) cloud echo-top frequency (shaded; %) and echo area coverage (solid line; %; right ordinate); and (bottom) sea surface temperature SST (black; °C; left ordinate), latent heat flux LH (red-solid line; W m^{-2}; right ordinate), and sensible heat flux SH×10 (red-dashed line; W m^{-2}; right ordinate) with composite means removed (i.e., SST′, LH′, and SH′, respectively). Composite date ranges include 7–13 Oct and 11–16 Nov 2011, respectively. Modified from *Ruppert and Johnson* [2015], supplemental figure, copyright 2015, with permission from the American Meteorological Society.

Figure 2. Model input sounding, based on the mean sounding from the DYNAMO–MJO2 suppressed phase (13–15 Nov 2011) from the R/V *Revelle*. (left) Skew T–log$p$ diagram, (center) zonal wind speed u (m s^{-1}), and (right) relative humidity RH (%; the vertical dashed line highlights the 50% level). CAPE (convective available potential energy; J kg^{-1}) is indicated (left panel), as is observed wind speed from the R/V *Revelle* mean sounding (thin line in center panel; smoothed with a 25-hPa running mean). Left and right ordinates are pressure (hPa) and height (km), respectively.

Figure 3. Large-scale vertical motion comparison: simulated w_{wtg} averaged over the second and third days of CTL (i.e. "w_{ctl}"); vertical motion from the DYNAMO northern sounding array averaged over SP/MJO2 ("w_{dynamo}"); and the vertical motion diagnosed from WTG balance using the apparent heat source Q_1 and static stability from DYNAMO during SP/MJO2 (i.e., "$w_{balanced}$") (mm s^{-1}).

Figure 4. Moisture tendencies [in Eulerian form; see equation (3)] averaged over the fourth and fifth days of CTL, including the net source ($\partial_t q$; black), the convective source ($-Q_2/L_v$; red), the source due to vertical advection ($-w_{wtg}\partial_z q$; orange), and the constant prescribed source ($\partial_t q_{psc}$; green). Values in parentheses are the corresponding column-integrated values (W m^{-2}).

Figure 5. Time–height series from CTL of (top) cloud-top frequency (shaded; %) and cloud area coverage (right ordinate; red; %); and (bottom) SST (black; left ordinate; °C) and domain-averaged rainfall (green; right ordinate; mm day^{-1}). The black-dashed line (top) indicates mixed-layer top, i.e., the level of minimum vertical eddy heat flux. The large abscissa ticks indicate 0000L, beginning with the simulation start at midnight on day 1 (D01). Three-point temporal boxcar smoothing has been applied to cloud-top frequency. The vertical gray-solid lines are provided for reference at the indicated times.

Figure 6. Potential temperature θ at 25 m (i.e., the lowest scalar level) with the horizontal average removed (θ'_{25m}; K; upper color bar), w at 225 m (w_{225m}; m s^{-1}; lower color bar), and cloud (i.e., columns where total cloud-liquid water path exceeds 5×10^{-3} mm; gray shading) from CTL at (a) 1200L and (b) 2100L D04, and (c) 1200L and (d) 2100L D05. No smoothing has been applied. About 50% of the total model domain is shown in each panel.

Figure 7. Time series from CTL of SST (black-solid; left ordinate; °C) and domain-averaged LH (blue) and SH×10 (red) (inner-right ordinate; W m^{-2}) and wind speed (WSPD) at the lowest scalar level (25 m) (outer-right ordinate; black-dashed-dotted; m s^{-1}). Open squares indicate the daily-mean (midnight–midnight) surface flux values, according to color.

Figure 8. Time–height series of heat-tendencies (see section 2.4) in CTL due to (a) total radiative heating Q_R and (b) convective heating Q_c (contoured every 0.5 K day^{-1}). Shown in (c) is w_{wtg} (contoured every 2 mm s^{-1}). Five-point boxcar smoothing has been applied to each variable in both time and height. The approximate cloud-top height (i.e., the upper 1.3% cloud-top frequency contour; Fig. 5) is included in (b). The arrows in (c) indicate the direction of w_{wtg} vertical motion. The zero-contour is dotted, here and henceforth. The time axis only spans D04–D07 for brevity and to emphasize detail in the diurnal cycle (here and henceforth).

Figure 9. As in Fig. 8 except with (a) Q_2/L_v (contoured every 0.5 g kg^{-1} day^{-1}), and (b) q' (shaded according to the color bar; 10^{-1} g kg^{-1}) and relative humidity RH (contoured every 5%).

Figure 10. (a) Column-integrated moisture budget in the Eulerian framework for CTL, according to (3), with the local time-tendency ($\partial_t \overline{q}$; black), prescribed tendency ($\partial_t \overline{q}_{psc}$; turquoise-solid), vertical-advective tendency ($w_{wtg}\partial_z \overline{q}$; turquoise-dot-dashed), surface evaporation (E_0; red-dashed), and the negative of surface precipitation ($-P_0$; red-solid) (left ordinate: mm day^{-1}); and (b) P_0 (repeated for detail; red; mm day^{-1}; left ordinate) and SST (black; °C; right ordinate). Multiplying terms in (a) by L_v yields energy units (right ordinate; W m^{-2}).

Figure 11. Cloud-top frequency (shaded; %; see Fig. 5 for color bar) and cloud area coverage (right ordinate; red; %) in (a) CTL, (b) FIXSST, (c) FIXSW, (d) NODC, (e) DBLSST, and (f) XCLDRAD.

Figure 12. Surface LH (solid) and SH (×10; dashed) (top; W m^{-2}) and SST (bottom; °C) for each sensitivity test, as indicated in the legend.

Figure 13. Vertical eddy buoyancy flux in (a) CTL, (b) FIXSST, (c) FIXSW, and (d) NODC (contoured every 3 W m^{-2}).

Figure 14. As in Fig. 10 except only showing (top) $w_{wtg}\partial_z\overline{q}$ and (bottom) P_0 for each sensitivity test, as indicated in the legend.

Figure 15. q' in (a) CTL, (b) FIXSST, (c) FIXSW, (d) NODC, (e) DBLSST, and (f) XCLDRAD (contoured every 0.5 10^{-1} g kg^{-1}).

Figure 16. Deviation of (top) longwave (LW) and (bottom) shortwave (SW) radiative heating rates averaged over cloudy columns from their respective domain-averaged tendencies in CTL (contoured every 0.5×10^{-1} K day^{-1}).

Figure 17. Conceptualized forcing mechanisms of the cumulus diurnal cycle – both the "forced" and "active" modes – over the tropical warm pool. (a) Time–height series of vertical eddy buoyancy flux (cf. Fig. 13a; smoothed to emphasize robust features), with large-scale subsidence indicated by the open arrows. (b and c, left) Schematized cloud scenes in the x–z plane at (b) 12L and (c) 21L, including relative humidity (shaded; warmer colors indicate drier air), surface fluxes (magenta arrows), eddy circulation (black arrows), cold pools (blue-dashed lines), and rainfall (light-blue lines). (b and c, right) Corresponding maps in the x–y plane of negative θ' at 25 m (blue), upward motion at 225 m (red), and cloud (gray–black) (directly from model output; cf. Fig. 6).

Table 1. List of the model simulations with name across the top row and the modifications ("mods") to shortwave (SW) warming, SST, or other indicated in the subsequent rows.

	CTL	FIXSW	FIXSST	NODC	DBLSST	XCLDRAD
SW mods	x	Fixed to 0621L	x	Fixed to 0621L	x	x
SST mods	x	x	Fixed to 29.9C	Fixed to 29.9C	Diurnal amplitude x 2	x
Other mods	x	x	x	x	x	No cloud-rad. feedbacks

Composite Diurnal Cycle in Two Suppressed Periods

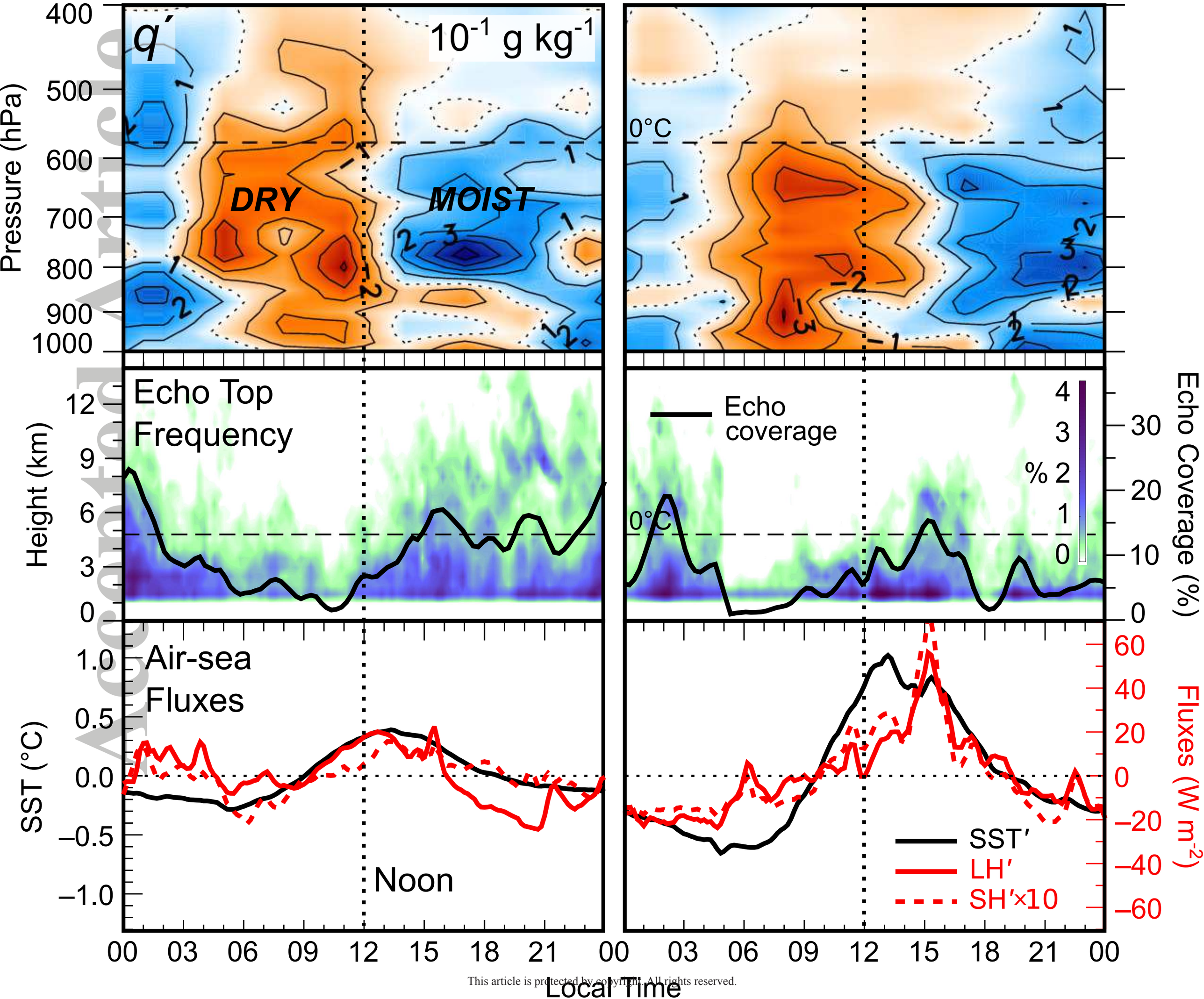

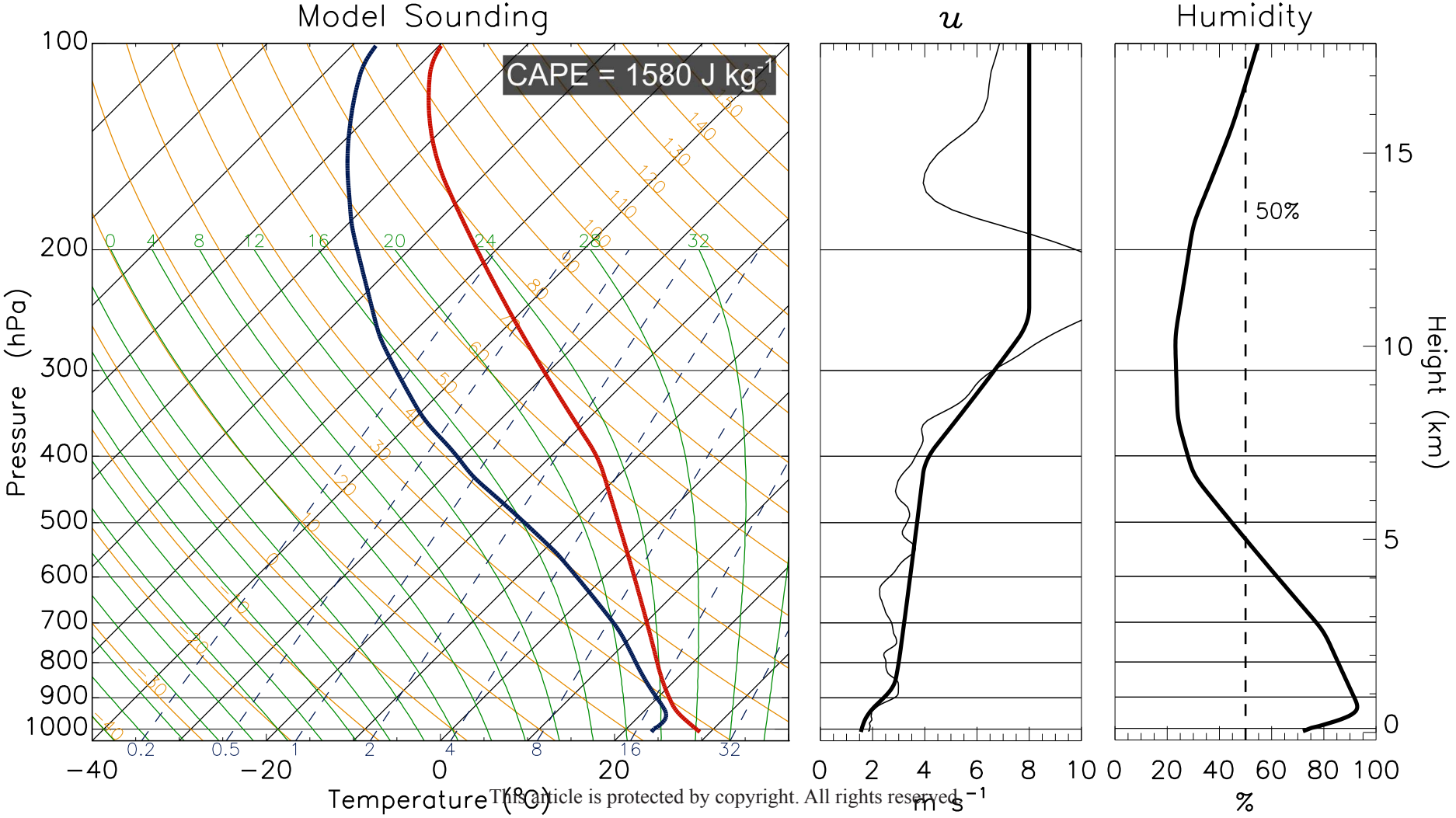

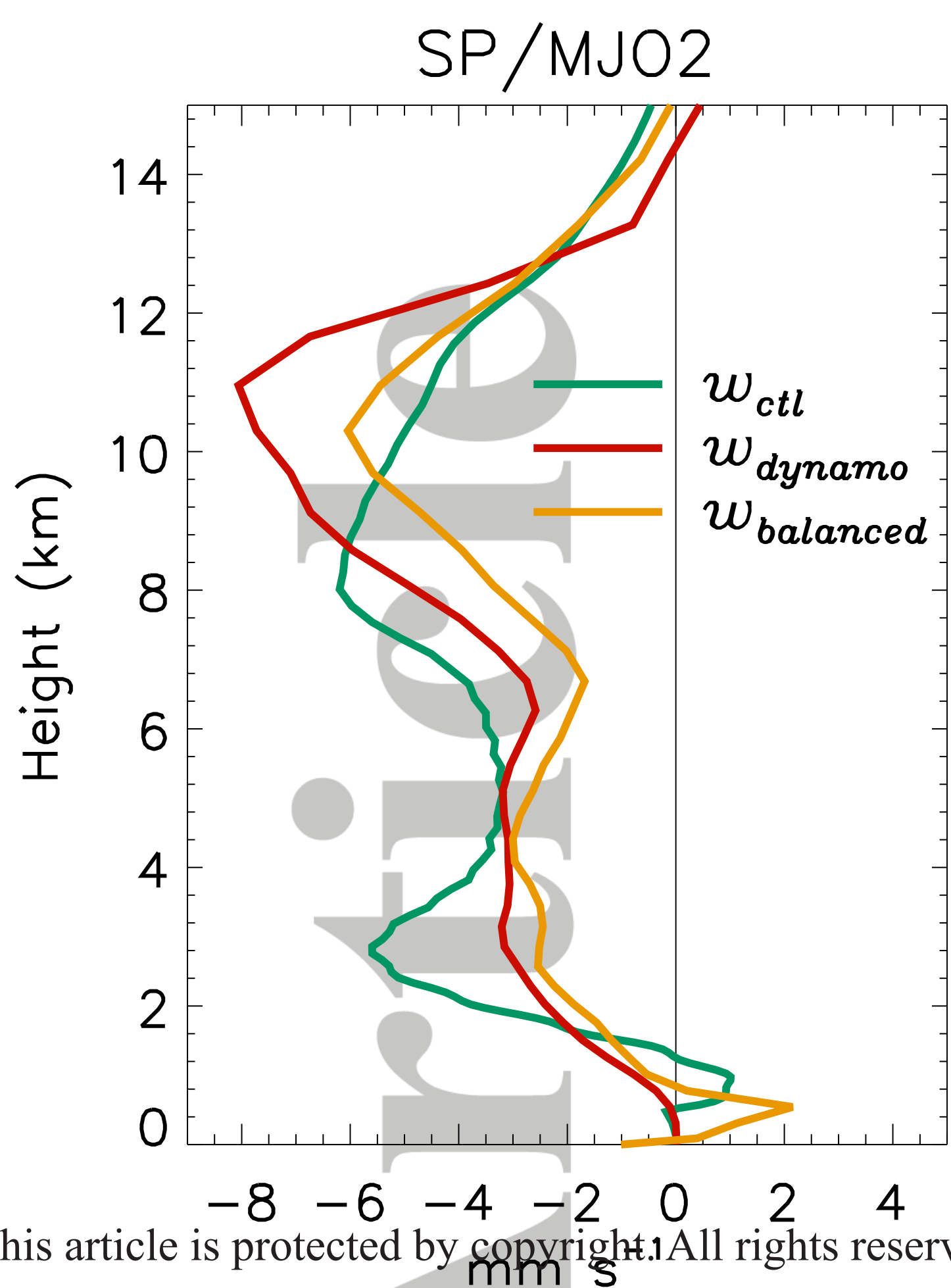

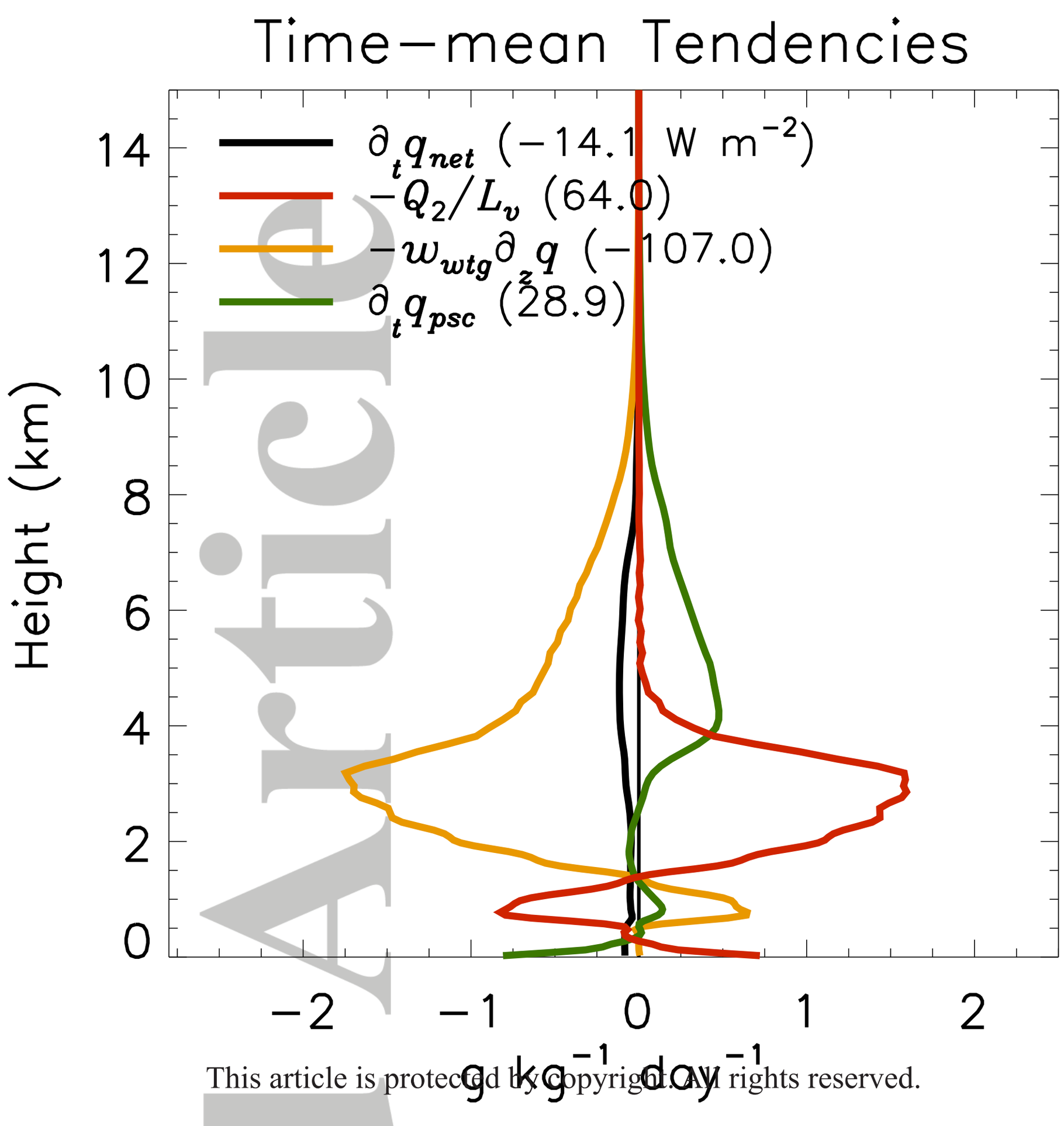

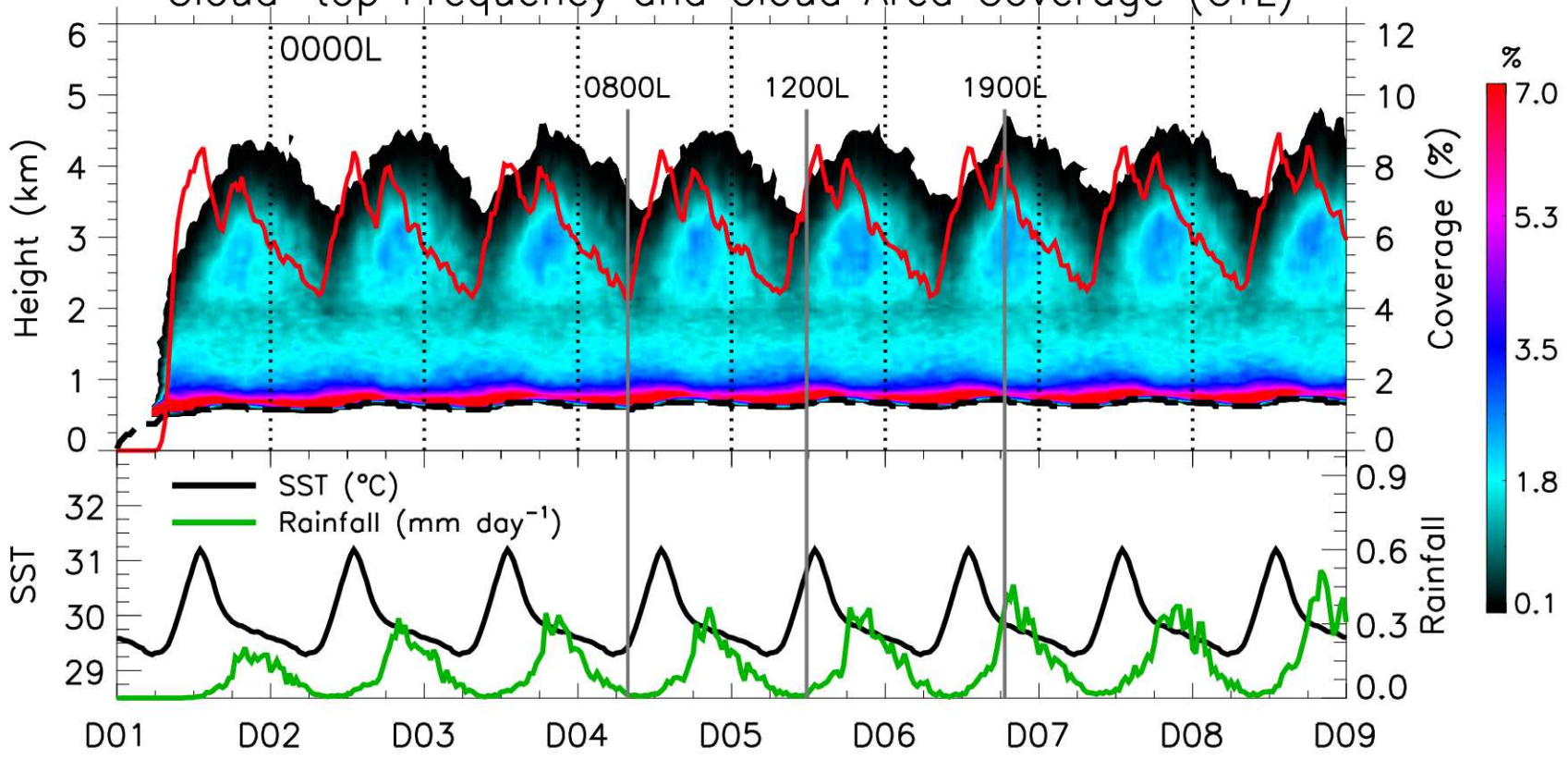

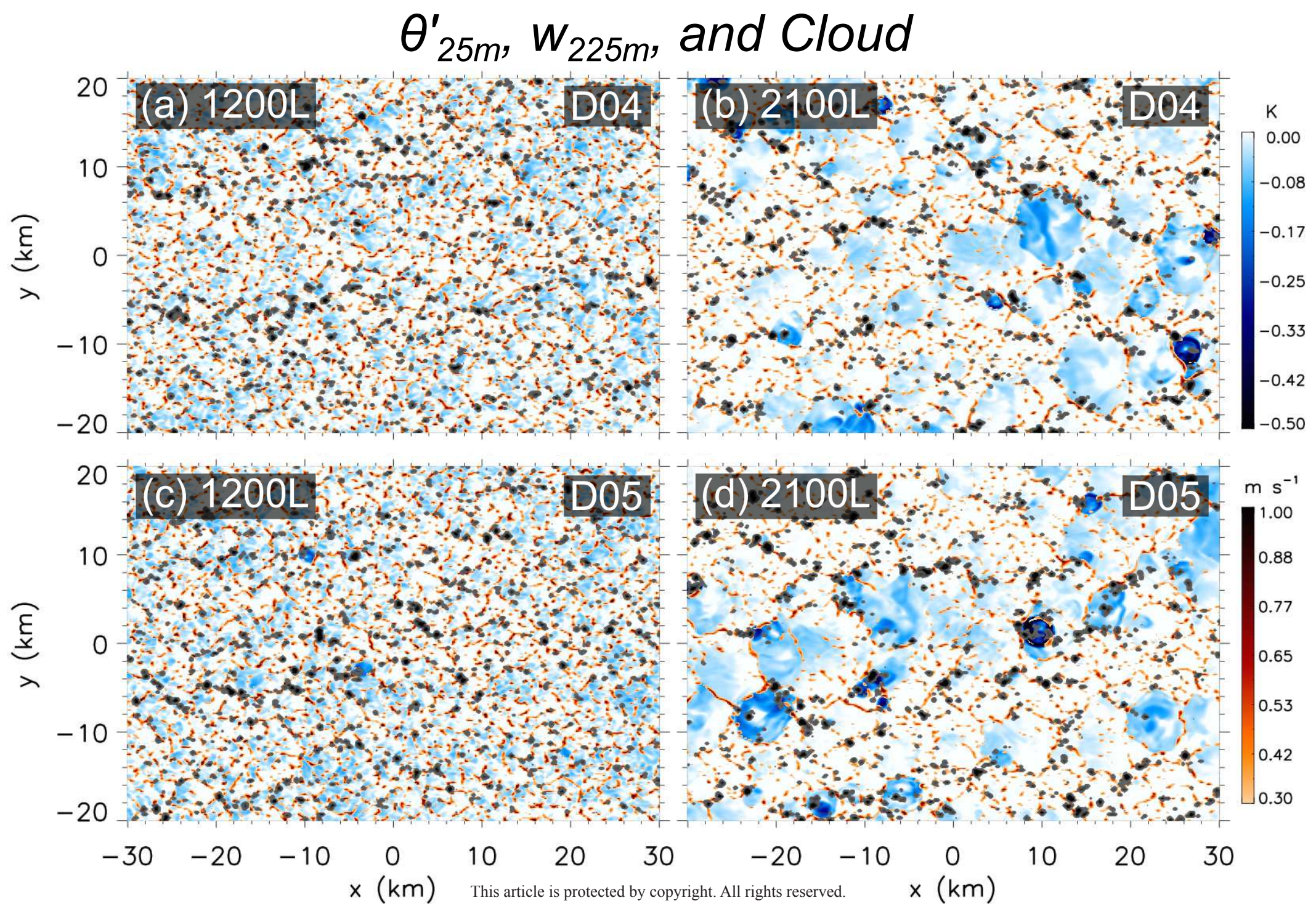

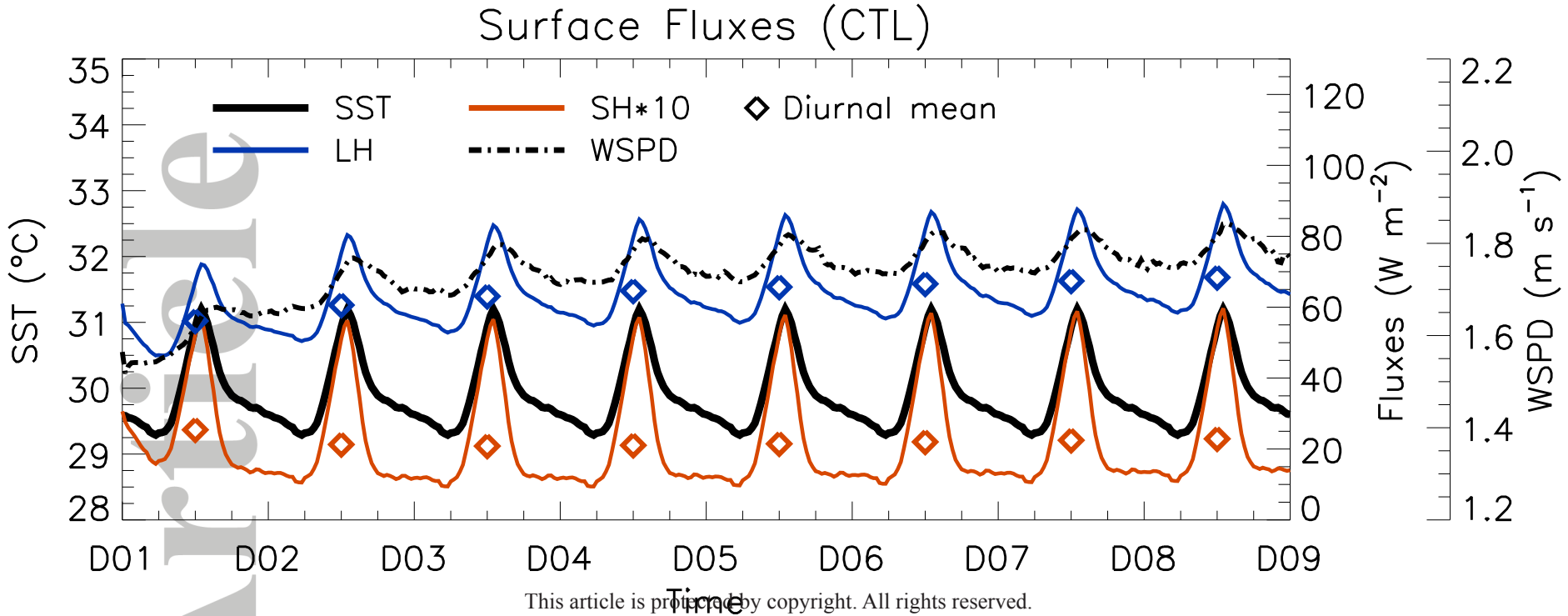

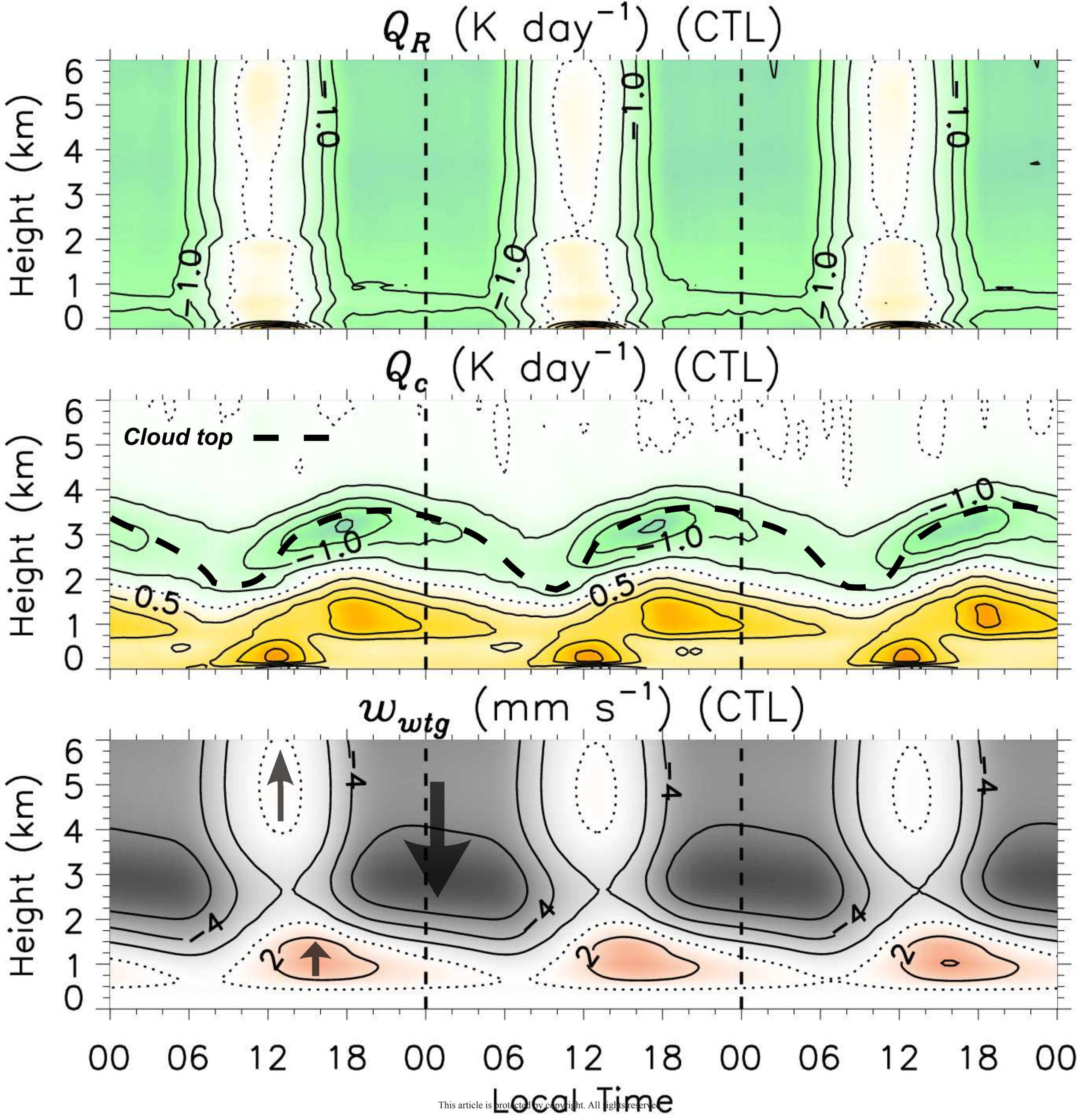

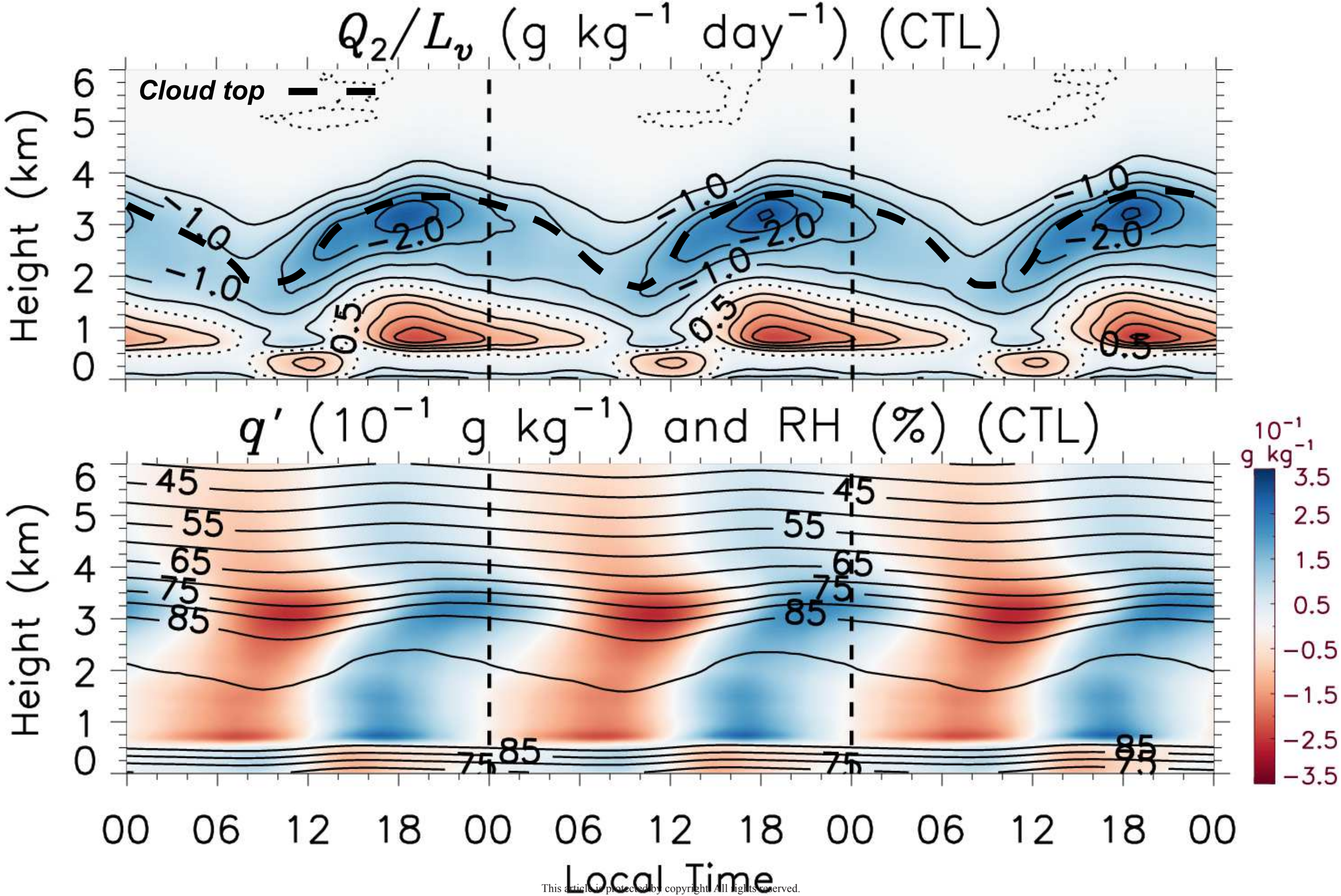

Moisture Budget (CTL)

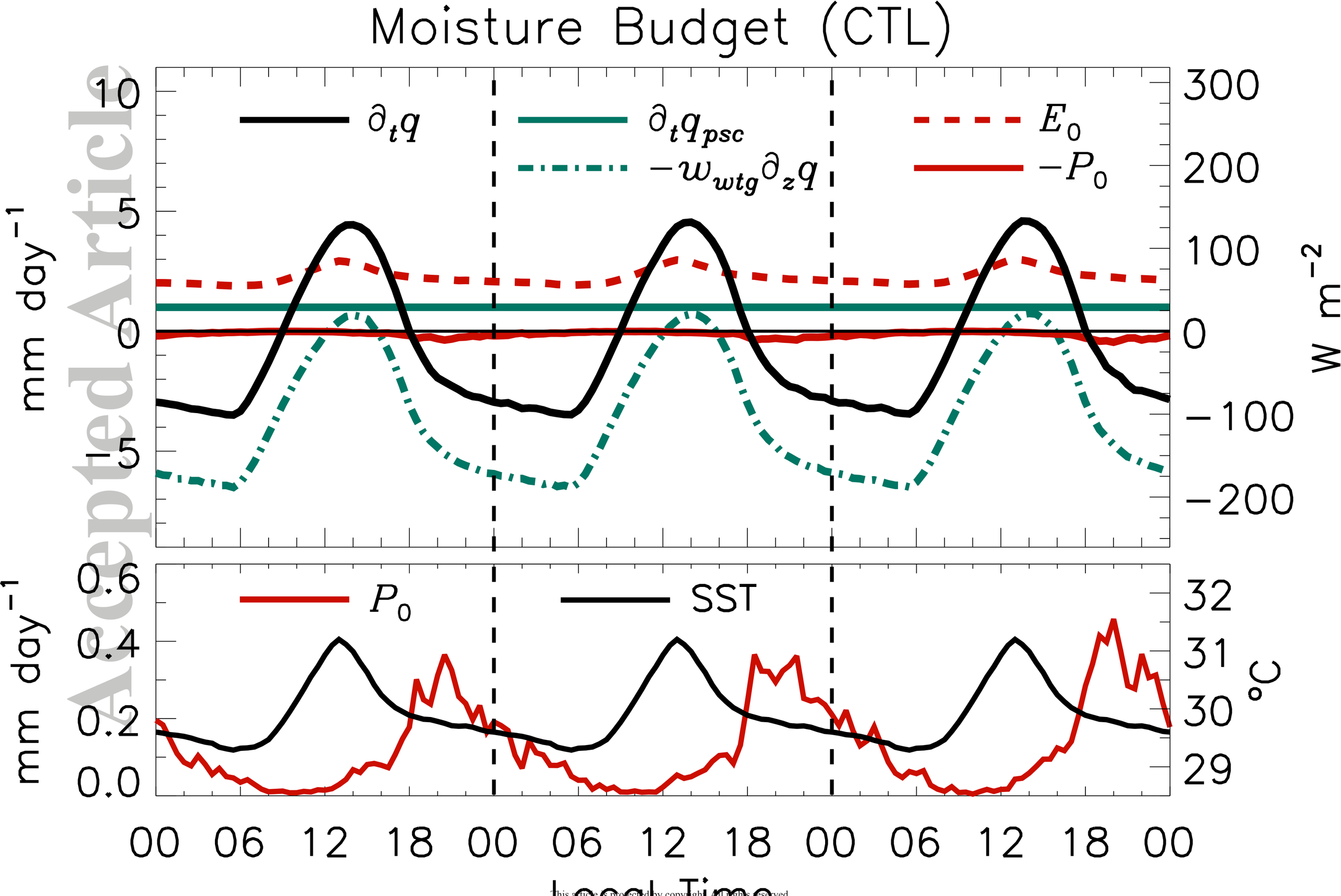

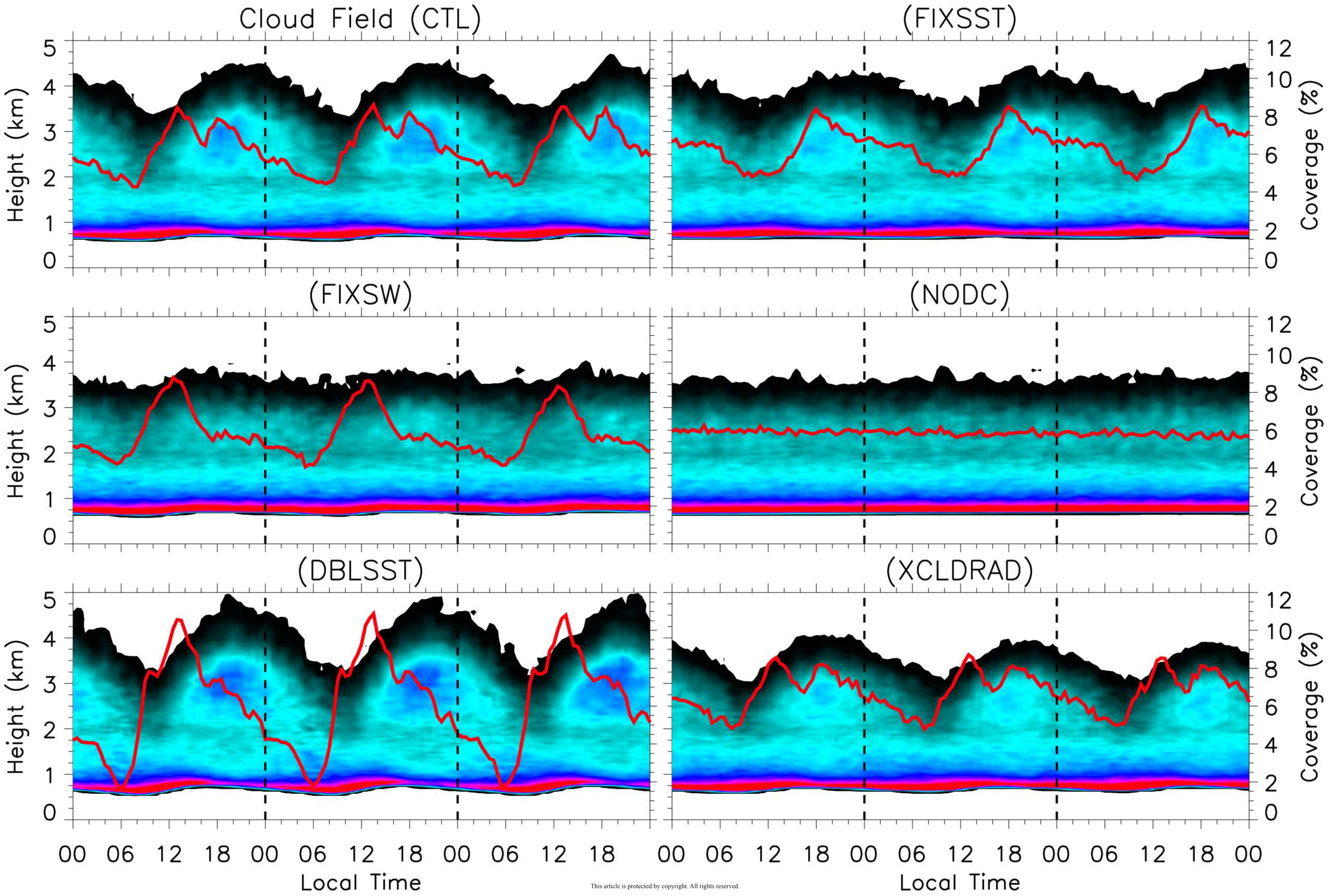

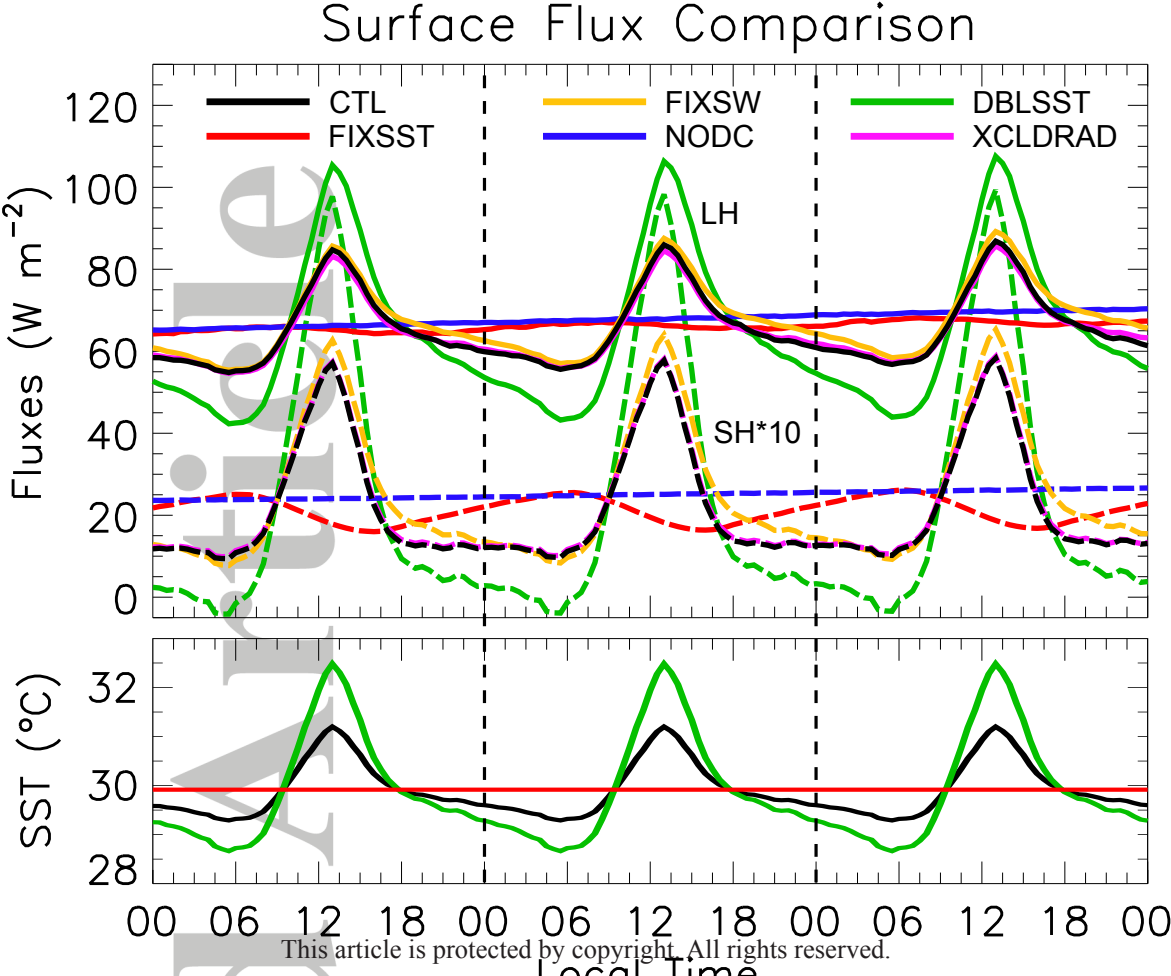

Vertical Eddy Buoyancy Flux (W m^{-2}) (CTL)

(FIXSST)

(FIXSW)

(NODC)

Height (km)

0 1 2 3 4 5

00 06 12 18 00 06 12 18 00 06 12 18 00

Local Time

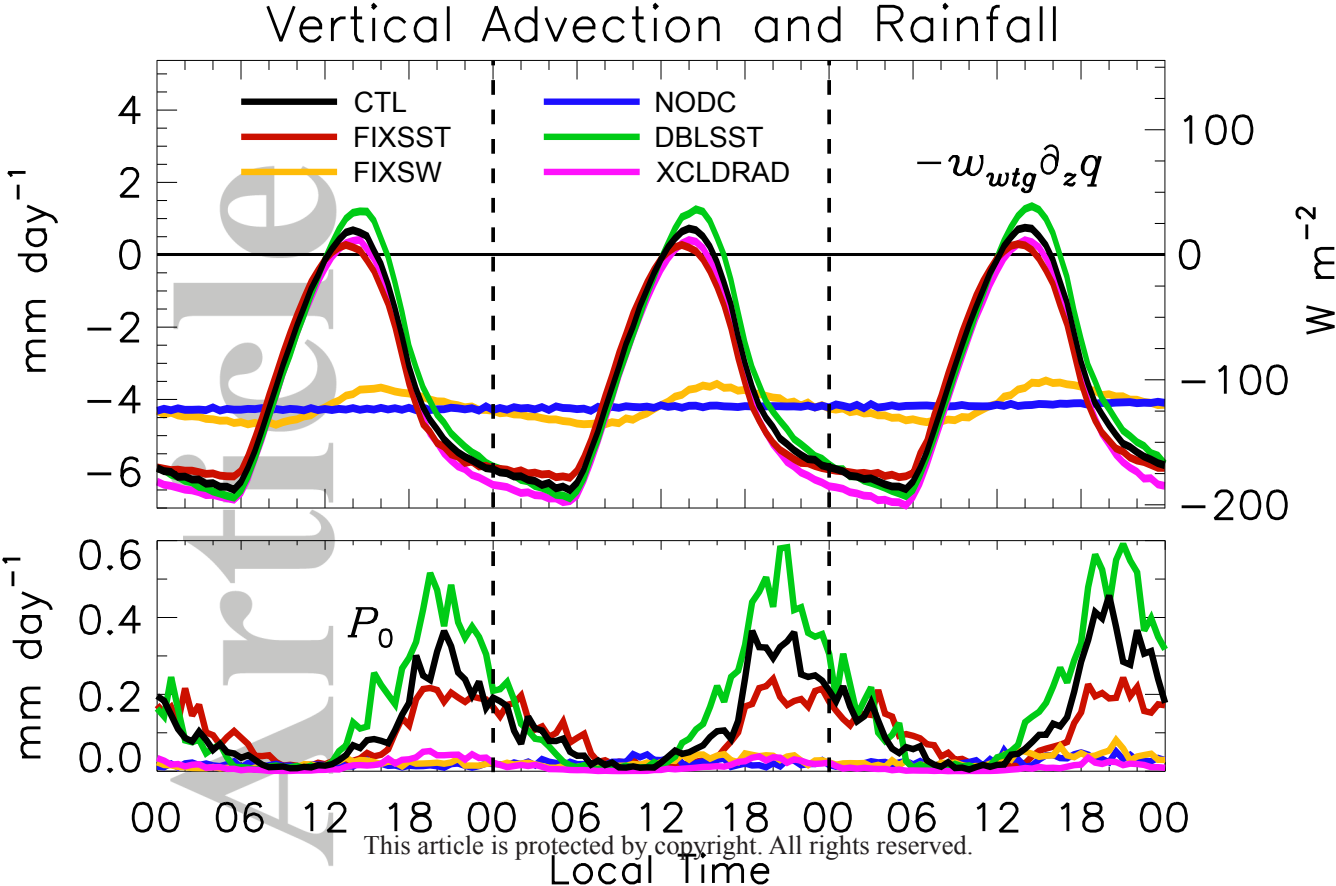

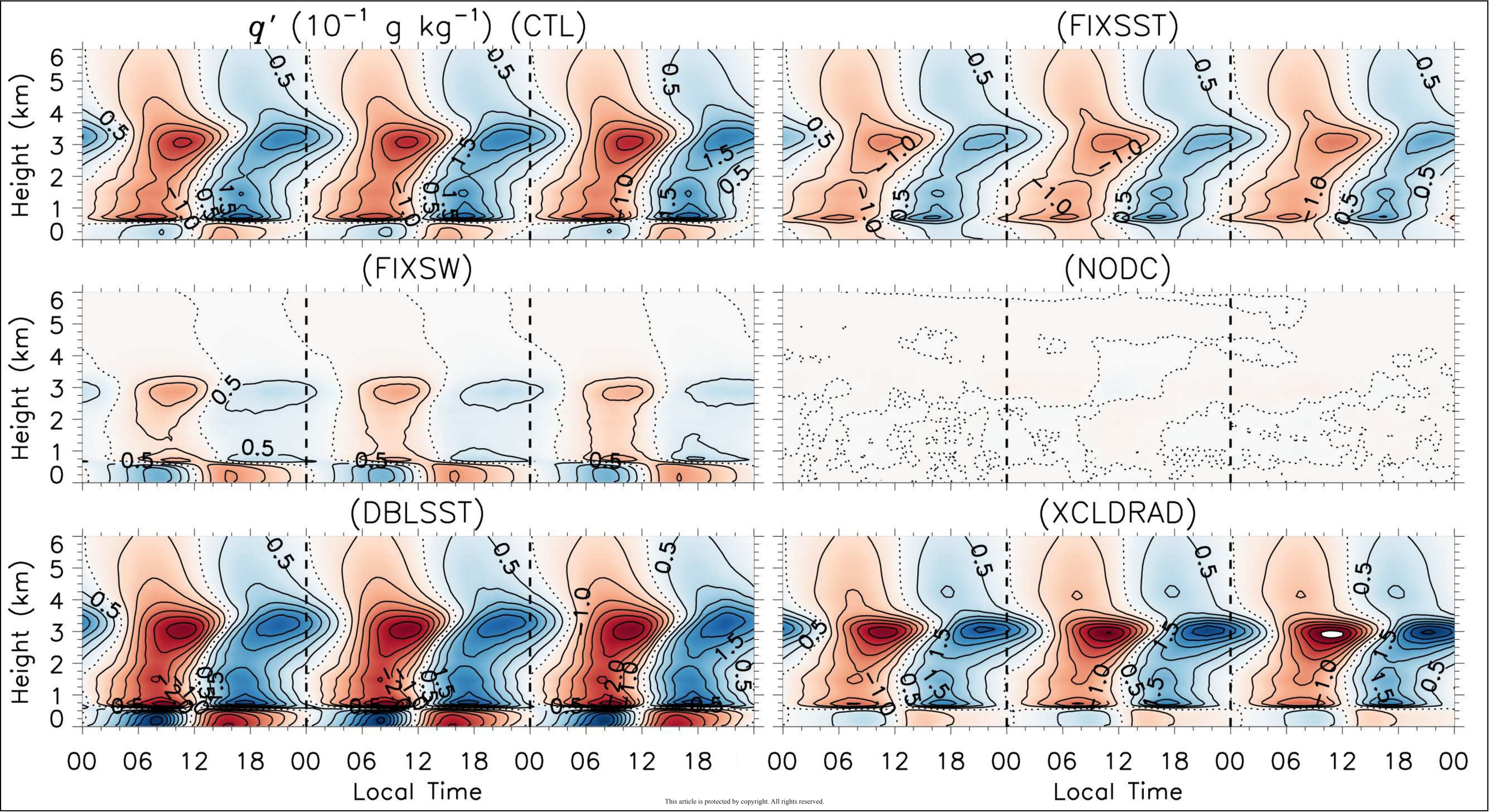

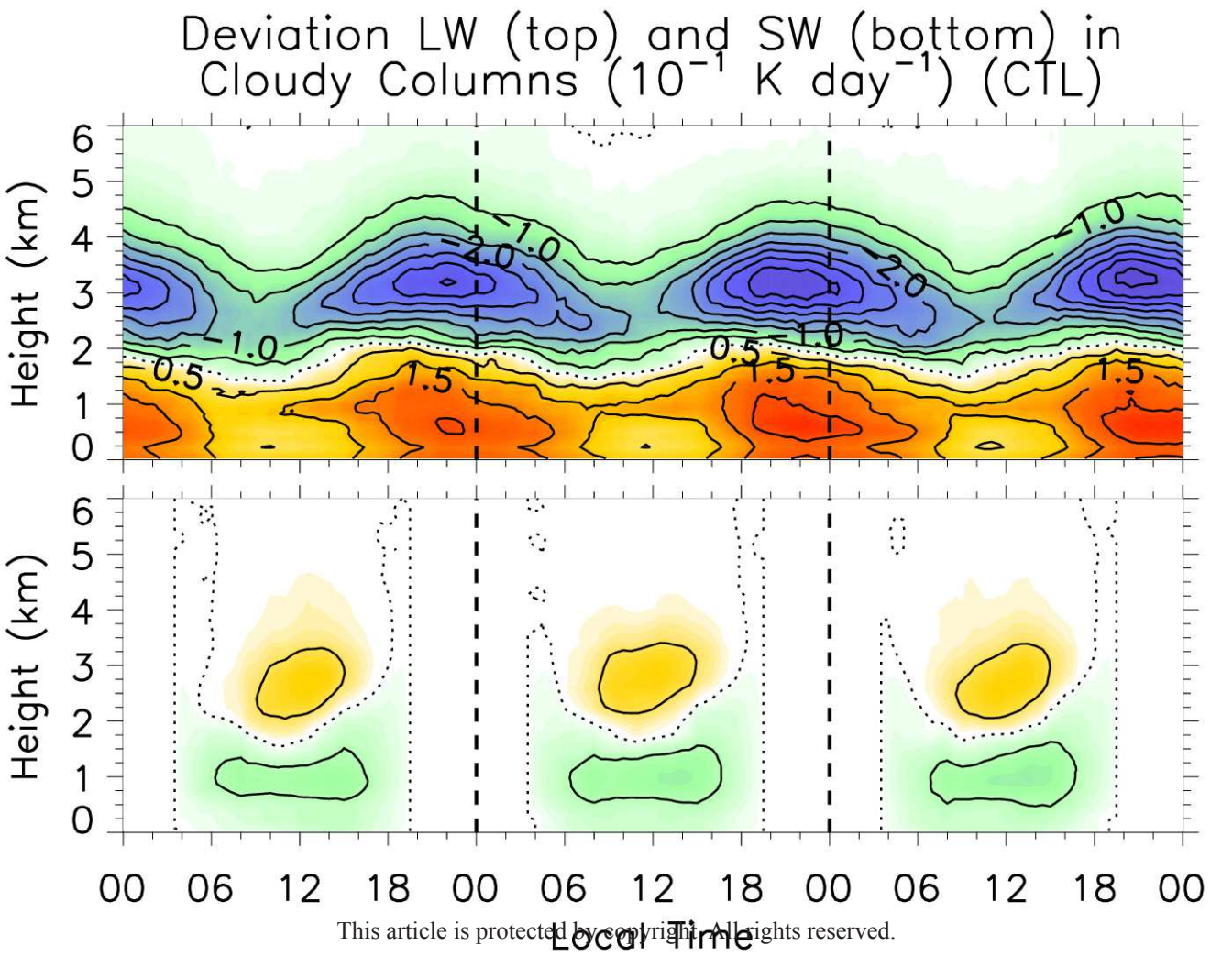

Mechanisms of Diurnal Cumulus Invigoration